A&A 571, A14 (2014)
DOI: 10.1051/0004-6361/201321562

Astronomy & Astrophysics
Special feature

Planck 2013 results

Planck 2013 results. XIV. Zodiacal emission

Planck Collaboration: P. A. R. Ade[88], N. Aghanim[61], C. Armitage-Caplan[92], M. Arnaud[74], M. Ashdown[71,6], F. Atrio-Barandela[19], J. Aumont[61], C. Baccigalupi[87], A. J. Banday[95,10], R. B. Barreiro[68], J. G. Bartlett[1,69], E. Battaner[97], K. Benabed[62,94], A. Benoît[59], A. Benoit-Lévy[26,62,94], J.-P. Bernard[95,10], M. Bersanelli[37,52], P. Bielewicz[95,10,87], J. Bobin[74], J. J. Bock[69,11], A. Bonaldi[70], J. R. Bond[9], J. Borrill[14,89], F. R. Bouchet[62,94], F. Boulanger[61], M. Bridges[71,6,65], M. Bucher[1], C. Burigana[51,35], R. C. Butler[51], J.-F. Cardoso[75,1,62], A. Catalano[76,73], A. Chamballu[74,16,61], R.-R. Chary[58], X. Chen[58], H. C. Chiang[29,7], L.-Y Chiang[64], P. R. Christensen[83,40], S. Church[91], D. L. Clements[57], J.-M. Colley[1,62], S. Colombi[62,94], L. P. L. Colombo[25,69], F. Couchot[72], A. Coulais[73], B. P. Crill[69,84], A. Curto[6,68], F. Cuttaia[51], L. Danese[87], R. D. Davies[70], P. de Bernardis[36], A. de Rosa[51], G. de Zotti[47,87], J. Delabrouille[1], J.-M. Delouis[62,94], F.-X. Désert[55], C. Dickinson[70], J. M. Diego[68], H. Dole[61,60], S. Donzelli[52], O. Doré[69,11], M. Douspis[61], X. Dupac[43], G. Efstathiou[65], T. A. Enßlin[79], H. K. Eriksen[66], F. Finelli[51,53], O. Forni[95,10], M. Frailis[49], A. A. Fraisse[29], E. Franceschi[51], S. Galeotta[49], K. Ganga[1,*], M. Giard[95,10], Y. Giraud-Héraud[1], J. González-Nuevo[68,87], K. M. Górski[69,98], S. Gratton[71,65], A. Gregorio[38,49], A. Gruppuso[51], F. K. Hansen[66], D. Hanson[80,69,9], D. Harrison[65,71], G. Helou[11], S. Henrot-Versillé[72], C. Hernández-Monteagudo[13,79], D. Herranz[68], S. R. Hildebrandt[11], E. Hivon[62,94], M. Hobson[6], W. A. Holmes[69], A. Hornstrup[17], W. Hovest[79], K. M. Huffenberger[27], A. H. Jaffe[57], T. R. Jaffe[95,10], W. C. Jones[29], M. Juvela[28], E. Keihänen[28], R. Keskitalo[23,14], T. S. Kisner[78], R. Kneissl[42,8], J. Knoche[79], L. Knox[31], M. Kunz[18,61,3], H. Kurki-Suonio[28,45], G. Lagache[61], A. Lähteenmäki[2,45], J.-M. Lamarre[73], A. Lasenby[6,71], R. J. Laureijs[44], C. R. Lawrence[69], R. Leonardi[43], J. Lesgourgues[93,86], M. Liguori[34], P. B. Lilje[66], M. Linden-Vørnle[17], M. López-Caniego[68], P. M. Lubin[32], J. F. Macías-Pérez[76], B. Maffei[70], D. Maino[37,52], N. Mandolesi[51,5,35], M. Maris[49], D. J. Marshall[74], P. G. Martin[9], E. Martínez-González[68], S. Masi[36], M. Massardi[50], S. Matarrese[34], F. Matthai[79], P. Mazzotta[39], P. R. Meinhold[32], A. Melchiorri[36,54], L. Mendes[43], A. Mennella[37,52], M. Migliaccio[65,71], S. Mitra[56,69], M.-A. Miville-Deschênes[61,9], A. Moneti[62], L. Montier[95,10], G. Morgante[51], D. Mortlock[57], S. Mottet[62], D. Munshi[88], J. A. Murphy[82], P. Naselsky[83,40], F. Nati[36], P. Natoli[35,4,51], C. B. Netterfield[21], H. U. Nørgaard-Nielsen[17], F. Noviello[70], D. Novikov[57], I. Novikov[83], S. Osborne[91], C. O'Sullivan[82], C. A. Oxborrow[17], F. Paci[87], L. Pagano[36,54], F. Pajot[61], R. Paladini[58], D. Paoletti[51,53], F. Pasian[49], G. Patanchon[1], O. Perdereau[72], L. Perotto[76], F. Perrotta[87], F. Piacentini[36], M. Piat[1], E. Pierpaoli[25], D. Pietrobon[69], S. Plaszczynski[72], E. Pointecouteau[95,10], A. M. Polegre[44], G. Polenta[4,48], N. Ponthieu[61,55], L. Popa[63], T. Poutanen[45,28,2], G. W. Pratt[74], G. Prézeau[11,69], S. Prunet[62,94], J.-L. Puget[61], J. P. Rachen[22,79], W. T. Reach[96], R. Rebolo[67,15,41], M. Reinecke[79], M. Remazeilles[70,61,1], C. Renault[76], S. Ricciardi[51], T. Riller[79], I. Ristorcelli[95,10], G. Rocha[69,11], C. Rosset[1], G. Roudier[1,73,69], M. Rowan-Robinson[57], B. Rusholme[58], M. Sandri[51], D. Santos[76], G. Savini[85], D. Scott[24], M. D. Seiffert[69,11], E. P. S. Shellard[12], G. F. Smoot[30,78,1], L. D. Spencer[88], J.-L. Starck[74], V. Stolyarov[6,71,90], R. Stompor[1], R. Sudiwala[88], F. Sureau[74], D. Sutton[65,71], A.-S. Suur-Uski[28,45], J.-F. Sygnet[62], J. A. Tauber[44], D. Tavagnacco[49,38], L. Terenzi[51], L. Toffolatti[20,68], M. Tomasi[52], M. Tristram[72], M. Tucci[18,72], J. Tuovinen[81], G. Umana[46], L. Valenziano[51], J. Valiviita[45,28,66], B. Van Tent[77], P. Vielva[68], F. Villa[51], N. Vittorio[39], L. A. Wade[69], B. D. Wandelt[62,94,33], D. Yvon[16], A. Zacchei[49], and A. Zonca[32]

(Affiliations can be found after the references)

Received 25 March 2013 / Accepted 4 March 2014

ABSTRACT

The *Planck* satellite provides a set of all-sky maps at nine frequencies from 30 GHz to 857 GHz. Planets, minor bodies, and diffuse interplanetary dust emission (IPD) are all observed. The IPD can be separated from Galactic and other emissions because *Planck* views a given point on the celestial sphere multiple times, through different columns of IPD. We use the *Planck* data to investigate the behaviour of zodiacal emission over the whole sky at sub-millimetre and millimetre wavelengths. We fit the *Planck* data to find the emissivities of the various components of the COBE zodiacal model – a diffuse cloud, three asteroidal dust bands, a circumsolar ring, and an Earth-trailing feature. The emissivity of the diffuse cloud decreases with increasing wavelength, as expected from earlier analyses. The emissivities of the dust bands, however, decrease less rapidly, indicating that the properties of the grains in the bands are different from those in the diffuse cloud. We fit the small amount of Galactic emission seen through the telescope's far sidelobes, and place limits on possible contamination of the cosmic microwave background (CMB) results from both zodiacal and far-sidelobe emission. When necessary, the results are used in the *Planck* pipeline to make maps with zodiacal emission and far sidelobes removed. We show that the zodiacal correction to the CMB maps is small compared to the *Planck* CMB temperature power spectrum and give a list of flux densities for small solar system bodies.

Key words. zodiacal dust – interplanetary medium – cosmic background radiation

* Corresponding author: K. Ganga, e-mail: ganga@apc.univ-paris-diderot.fr

1. Introduction

This paper, one of a set associated with the 2013 release of data from the *Planck*[1] mission (Planck Collaboration I 2011), describes the measurement of zodiacal emission with *Planck*.

Zodiacal light, the reflection of sunlight by small dust particles in our Solar System, can be seen by eye at dawn or dusk in dark locations, and contributes significantly to the diffuse sky brightness at optical and near-infrared wavelengths. In recent decades the study of zodiacal emission, or the thermal re-emission of absorbed energy from these interplanetary dust (IPD) particles, has been enabled by the advent of infrared astronomical techniques, and it is now known to dominate the diffuse brightness of most of the sky between 10 and 50 μm (see, for example, Leinert et al. 1997).

Full-sky, infrared satellite surveys in particular have allowed us to begin to determine the structure of the density of the IPD (Hauser et al. 1984; Kelsall et al. 1998; Fixsen & Dwek 2002; Pyo et al. 2010). The full-sky model of zodiacal emission from the Cosmic Background Explorer Diffuse Infrared Brightness Experiment (COBE/DIRBE) team (Kelsall et al. 1998, hereafter K98) is commonly used at longer wavelengths, and is easily adapted for *Planck*. Other models are presented in Good et al. (1986), Rowan-Robinson et al. (1990, 1991), Jones & Rowan-Robinson (1993), Vrtilek & Hauser (1995), Wright (1998), and Rowan-Robinson & May (2013). The K98 model comprises the well-known diffuse cloud, three sets of dust bands, first discovered by IRAS (Low et al. 1984), and a circumsolar ring and Earth-trailing feature, hinted at in IRAS and confirmed by DIRBE (called a "blob" in K98. See Reach et al. 1995, and references therein).

Fixsen & Dwek (2002) used data from COBE's Far Infrared Absolute Spectrophotometer (FIRAS) to extend measurements of the diffuse cloud to longer wavelengths, but given FIRAS' modest angular resolution and large uncertainties in the submillimetre region, they could not say more about zodiacal features on small angular scales. *Planck*'s sensitivity allows it to detect and measure the emissivity of the diffuse zodiacal cloud at long wavelengths, and its angular resolution allows it to characterize the smaller-scale components of the zodiacal emission.

This paper is structured as follows: Sect. 2 describes relevant aspects of the *Planck* mission, including its observing strategy and data processing; Sect. 3 describes how *Planck* detects zodiacal emission; Sect. 4 describes the COBE zodiacal emission model; Sect. 5 describes how we fit that model to the *Planck*/HFI data; and Sect. 6 gives the results of the fit. Section 7 gives our conclusions.

2. The *Planck* mission

Planck, launched in May 2009, comprised two instruments: the Low Frequency Instrument (LFI), which observed at 30, 44 and 70 GHz, and the High Frequency Instrument (HFI), which observed at 100, 143, 217, 353, 545, and 857 GHz. The mission is described in Planck Collaboration I (2014). This work uses data only at frequencies of 100 GHz and higher. At these frequencies, *Planck*'s angular resolution ranges from 9.′7 to 4.′6 (Planck Collaboration VII 2014).

[1] *Planck* (http://www.esa.int/Planck) is a project of the European Space Agency (ESA) with instruments provided by two scientific consortia funded by ESA member states (in particular the lead countries France and Italy), with contributions from NASA (USA) and telescope reflectors provided by a collaboration between ESA and a scientific consortium led and funded by Denmark.

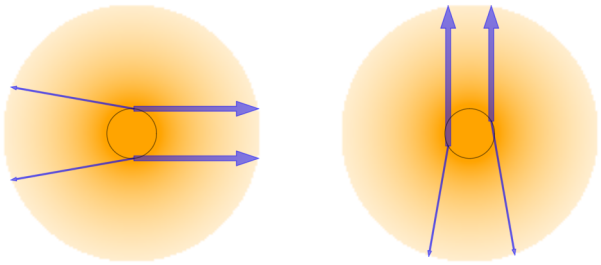

Fig. 1. Schematic representation of the geometry of *Planck*'s measurements, which shows that it can view different amounts of zodiacal emission while looking at the same point on the distant sky. Observations of two points on the sky are shown, each with two measurements of the given point. The plane of the Ecliptic is in the plane of the diagram. The Sun is in the centre of each panel. The solid black ring represents the orbit of the Earth and *Planck*. The orange circle represents the IPD cloud, cut off at the orbit of Jupiter, beyond which we assume there is no contribution to the zodiacal emission. *Left*: case where the phase of the scan cycloid and the location of the observed point on the sky (towards the right of the page in this case) yield two measurements for which the lines of sight through the IPD are roughly equal, and the same zodiacal signal is seen. *Right*: case where the phase of the scan cycloid and the location of the observed point on the sky (now towards the top of the page) yield different total columns of IPD along the lines of sight, and thus a different zodiacal signal. *Note that this figure is highly stylized and not to scale.*

2.1. Orbit, scanning strategy, and dates of observation

The *Planck* orbit, scanning strategy, and dates of observation for various subsets of the data are described in detail in Sect. 4.1 of Planck Collaboration I (2014). The spin axis lies 7.°5 from the Sun-Earth vector, moving around the anti-Sun point in a cycloid of period six months. This cycloid component results in differing total amounts of IPD in *Planck*'s line of sight for different observations of the same point on the distant celestial sphere, as shown schematically in Fig. 1.

As detailed in Planck Collaboration I (2014), the *Planck* beams scan the entire sky exactly twice in one year, but scan only 93% of the sky in six months. For convenience, we call an approximately six month period one survey (Table 1 in Planck Collaboration I 2014), and use that term as shorthand for one coverage of the sky. The "nominal" mission comprises the first two surveys and part of the third. During any single one of these surveys, some pixels near the ecliptic poles are observed multiple times, as are the pixels near the ecliptic plane that are seen both at the beginning and at the end of the survey. The bulk of the sky, however, is observed only during well-defined periods of approximately one week. Figure 2 shows the Julian dates of observations of those pixels on the sky for which the observation times during Survey 1 spanned one week or less. The equivalent figure for Survey 2 is similar. The scanning strategies for Surveys 3 and 4 were almost identical to those of Surveys 1 and 2, respectively.

2.2. Data processing

HFI data processing is described in Planck HFI Core Team (2011) and Planck Collaboration VI (2014). Given the time-dependent nature of the zodiacal signal seen with the *Planck* scanning strategy, the analysis in this paper is based on individual Survey 1–4 maps. This allows us to exclude from the analysis

Table 1. Zodiacal bands identified by COBE and IRAS, and information about the asteroid families with which they have been associated.

COBE		IRAS		Associated asteroid family				
Name[a]	δ_ζ[b]	name[c]	i_p[d]	name[e]	i_p[f]	type[g]	age[h]	a[i]
1	8.78	γ	9.35	490 Veritas	9.26	C/Ch/...	8.3	3.169
2	1.99	α	1.34	656 Beagle	1.34	.../.../C	$\lesssim$10	3.157
		β	2.11	832 Karin	2.11	.../.../S	5.8	2.866
3	15.0	J/K	12.0	845 Naema	11.96	.../C/...	$\gtrsim$20	...
				4562 Iannini	12.17	.../.../S	$\lesssim$5	2.644
		M/N	15.0	1521 Seinajoki	15.02	.../.../...	...	2.852

Notes. [(a)] K98 band designation. [(b)] δ_ζ parameter of the K98 zodiacal emission model. This parameter determines roughly at which ecliptic latitudes, in degrees, the band appears. [(c)] IRAS bands associated with the given COBE band. [(d)] Modelled proper inclination of the given IRAS band. The first three are from Grogan et al. (2001), while the last two are from Sykes (1988). [(e)] Asteroid family associated with the given IRAS band. These all come from N03, except that for 832 Karin, which comes from N08. [(f)] Average proper inclination for the associated asteroid family. These all come from N03, except that for 832 Karin, which comes from N08. [(g)] Spectral type/classifications. The first two entries in the triplets correspond to the Tholen and SMASSII classes Bus & Binzel (2002), while the third corresponds to the SDSS-based classification (Carvano et al. 2010). Ellipses are used to indicate that the given classification was not found. [(h)] Time since the asteroid disruption that created the associated asteroidal family, in Myr. These come from N03, except for 832 Karin, which comes from N08. [(i)] Proper semi-major axis of the asteroidal family associated with the band, in AU. These come from N03, except for 832 Karin, which comes from N08.

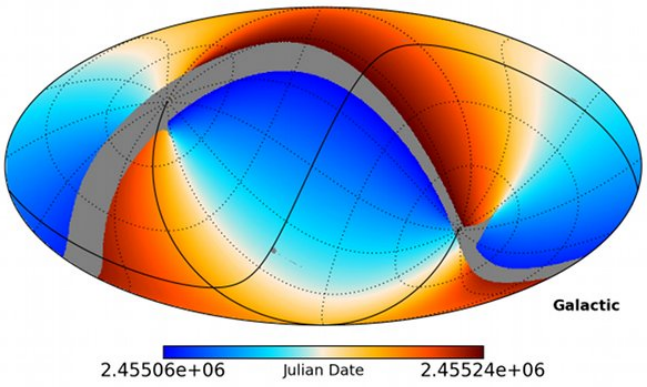

Fig. 2. Julian date of observation of pixels on the sky during Survey 1, for a single detector, in Galactic coordinates. There are only very small differences between maps for different detectors. The grid lines show ecliptic coordinates, with the darker lines representing the ecliptic plane and the line of zero ecliptic longitude. Undefined pixels, which were either not observed at all, or which were observed multiple times over a period that spanned more than one week and are thus not used in this analysis, are shown as the uniform grey band.

regions of the sky and periods of time where the column of IPD viewed by *Planck* is not constant.

The HFI instrument has multiple horns at each frequency (Planck Collaboration VII 2014, Fig. 9). Working with individual horn maps, rather than co-added frequency maps, allows us to adjust the response of each detector for uniform response to the zodiacal spectrum, rather than to the cosmic microwave background (CMB) spectrum, as is done in the standard processing (Planck Collaboration IX 2014). At 100, 143, 217, and 353 GHz, some horns couple to two polarization sensitive bolometers (PSBs; Jones et al. 2003). As we are not addressing polarization here, we simply average the maps from a PSB pair.

As the evaluation of the model to be presented in Sect. 4 involves calculating emission from a number of points along each line of sight and summing them, the computations are time consuming. To mitigate this to some extent, we use 13.′7 × 13.′7 pixels (`HEALPix` $N_{\rm side}$ = 256; Górski et al. 2005), rather than the original 1.′7 × 1.′7 HFI pixels ($N_{\rm side}$ = 2048), thereby reducing the number of map pixels from 50 million to less than 800 thousand. Although this reduces our sensitivity to finer-scale structures, it does not hinder comparisons with DIRBE, which had a still larger beam. Smaller pixels will be used in future work, as more detail is teased out of the data.

Pre-launch estimates of *Planck*'s ability to detect zodiacal emission and an estimate of the possible level of contamination at the highest *Planck* frequencies were presented in Maris et al. (2006). More recent predictions have addressed the possibility of zodiacal contamination at lower frequencies (Diego et al. 2010), and speculated that emission from dust in the outer solar system might contribute to the large-scale anomalies reported in data from the *Wilkinson* Microwave Anisotropy Probe (WMAP) at large angular scales (Maris et al. 2011; Hansen et al. 2012).

3. Detection

The existence of the zodiacal emission in the *Planck* maps is straightforward to demonstrate by exploiting the fact, noted above, that different *Planck* surveys sample different columns of IPD while observing the same location on the distant celestial sphere. Figure 3 shows Survey 1 and Survey 2 maps for the 857–1 detector, and their difference. (See Figs. 10 and 11 for similar figures for all HFI frequencies.) Three features stand out in the map difference: (1) the scale has been reduced immensely, but the Galactic plane is still visible; (2) the "arcs" at the top and the bottom of the difference map are the images of the Galactic centre as seen through the instruments' far sidelobes (FSLs); and (3) the zodiacal emission can be seen as the variations following the ecliptic plane.

In the difference map, zodiacal emission is seen in the ecliptic plane as both positive and negative, depending upon the relative geometry of the IPD and the *Planck* satellite when a given location was observed in the two surveys. While taking the survey difference reduces the amplitude of the zodiacal emission signal (this will be described in Sect. 4, and in particular Fig. 4;

see also Maris et al. 2006), it has the advantage that most of the Galactic and extra-galactic signals, the main contaminants in the analysis at high frequencies, are removed as well. What remains of the Galactic signal arises from effects such as beam asymmetries and imperfections in the transfer function removal (Planck Collaboration VII 2014). The conclusions of this analysis remain the same for Galactic cuts of anywhere between 5° and 20°. We generally do not use data within 10° of the Galactic plane, in order to avoid the most visible of the Galactic contamination visible in the bottom panel of Fig. 3. We emphasize that analysing difference maps makes this work less sensitive to Galactic contamination than some other *Planck* analyses.

It should be noted that the zodiacal emission is much dimmer than many other background components in the *Planck* data. Whereas the zodiacal emission dominates the sky in some IRAS and COBE bands, this is never the case for *Planck*, where the cosmic infrared background and Galactic dust dominate at high frequencies, and the CMB itself dominates at lower frequencies. This makes our differencing scheme appealing, but also restricts the analysis in some ways. It is, for example, difficult to look at individual scans, or slices of the sky, as has been done successfully with IRAS. We are obligated to use almost the entire sky, and to use a model of the zodiacal emission to interpret variations, rather than being able to directly interpret the total zodiacal emission on the sky.

4. Model

This section describes the creation of the zodiacal and far sidelobe templates that we fit to the survey difference map in Fig. 3.

4.1. Zodiacal components

The COBE/DIRBE zodiacal emission model is described in depth in K98, but we review the salient parts here.

4.1.1. Diffuse cloud

The density of the diffuse IPD cloud, having both radial and vertical dependence, is taken to be of the form

$$n_{\rm c}(\boldsymbol{R}) = n_0 R_{\rm c}^{-\alpha} \begin{cases} {\rm e}^{-\beta\left(\zeta^2/2\mu\right)^{\gamma}} & \text{if } \zeta < \mu \\ {\rm e}^{-\beta(\zeta-\mu/2)^{\gamma}} & \text{if } \zeta \geq \mu, \end{cases} \quad (1)$$

where

$$R_{\rm c} = \sqrt{(x-x_0)^2 + (y-y_0)^2 + (z-z_0)^2}, \quad (2)$$

$$\zeta \equiv |Z_{\rm c}| / R_{\rm c}, \quad (3)$$

$$Z_{\rm c} = (x-x_0)\sin(\Omega_R)\sin(i_R) - (y-y_0)\cos(\Omega_R)\sin(i_R) + (z-z_0)\cos(i_R), \quad (4)$$

and α, β, γ, μ, x_0, y_0, z_0, Ω_R, and i_R are parameters describing the location and shape of the cloud. This form (and others used elsewhere that are similar) is based on an approximation of a model of particles orbiting the Sun, accounting for drag from the Poynting-Robertson effect, and with a modified fan distribution used to describe the changes in density above and below the plane of the ecliptic. See K98 for details and references.

The numerical values for the parameters can be found in K98, or from the LAMBDA website[2]. This is shown, for both Survey 1 and Survey 2, as well as their difference, in the bottom row of Fig. 4. These plots were made assuming that the particles emit as blackbodies, which is only an approximation, as we will see in Sect. 5.

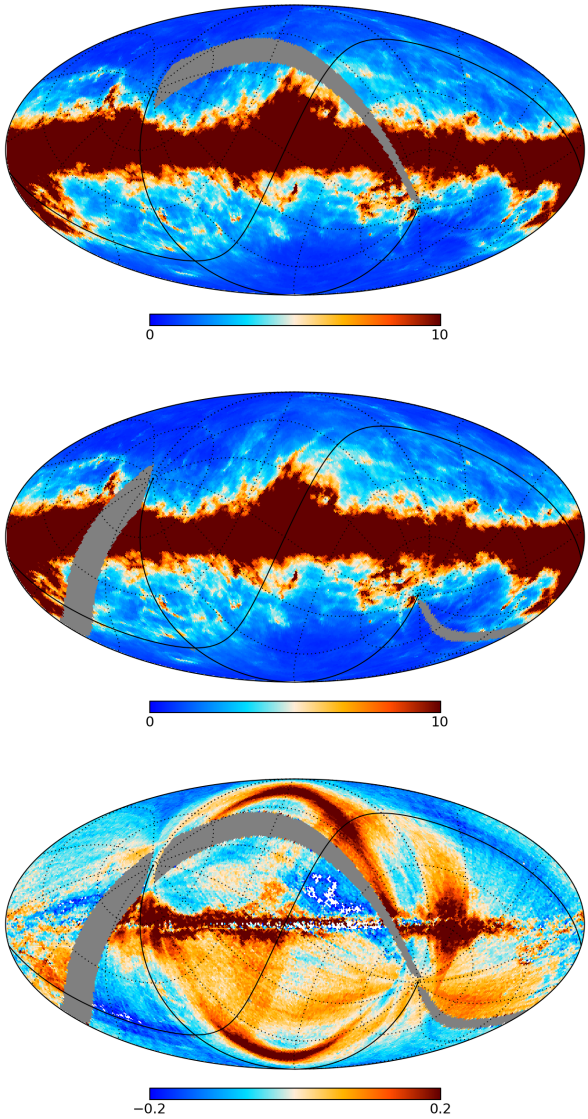

Fig. 3. Single-survey maps in Galactic coordinates for the 857-1 detector. *Top*: Survey 1 map. *Middle*: Survey 2 map. *Bottom*: Survey 2 minus Survey 1 difference map. This bottom image shows the zodiacal emission and the residual Galactic emission effects that are discussed in the text. The units are MJy sr^{-1}, assuming a spectrum inversely proportional to frequency. Undefined pixels are shown in grey. These occur in pixels that either have not been observed during the survey, were observed during the passage of a planet, or for a small number of other events. In the top two plots, pixels that were observed over periods longer than a week were not masked, and thus the masked regions are smaller in the top two images than that in the difference (*bottom*) panel. The units are MJy/sr.

4.1.2. Dust bands

The zodiacal dust bands were first seen by IRAS (Low et al. 1984), and appear as pairs of bright, parallel bands equally spaced above and below the ecliptic plane. They were quickly associated with asteroid families, and then understood to be the

[2] Legacy Archive for Microwave Background Data Analysis – NASA (http://lambda.gsfc.nasa.gov/)

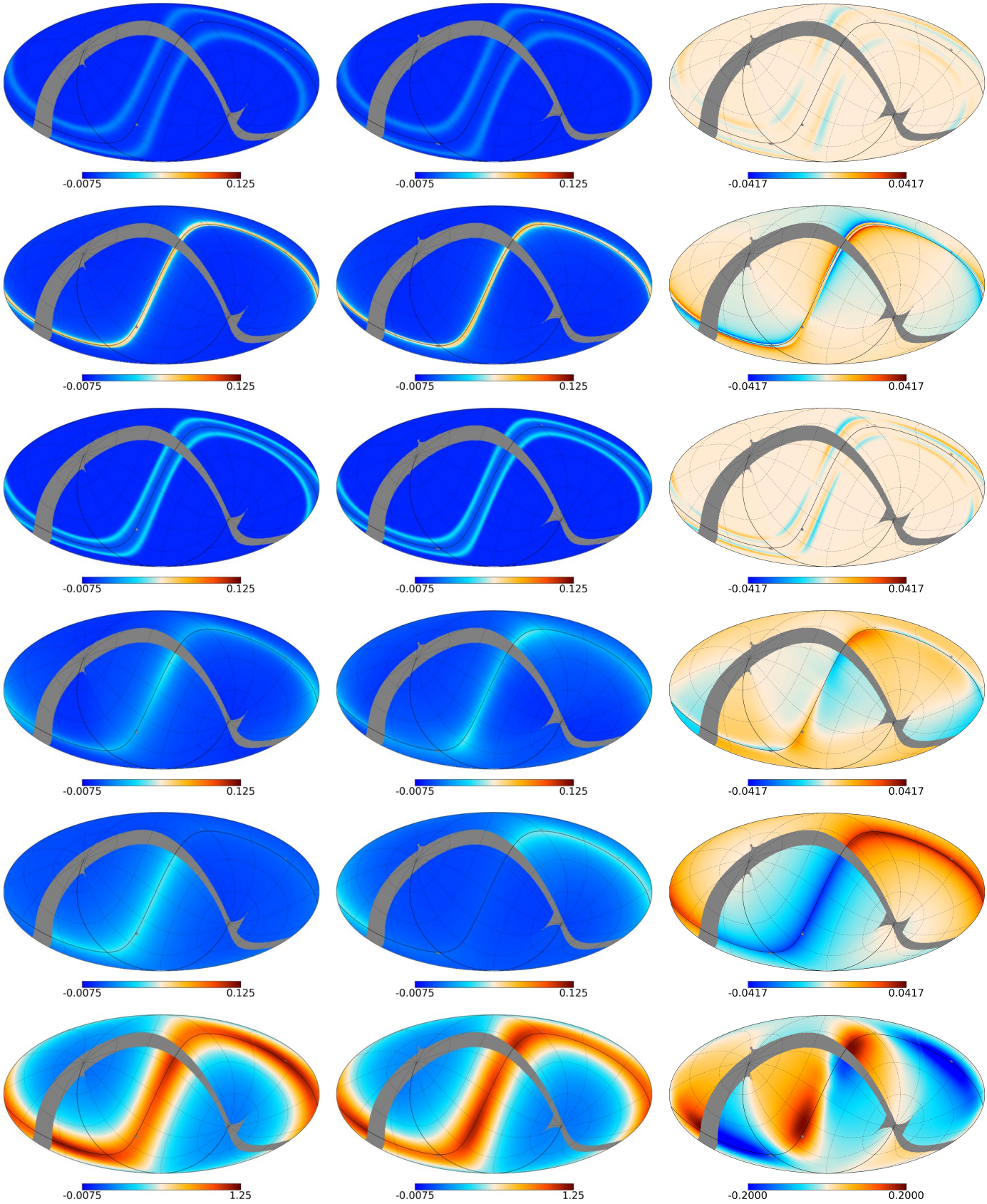

Fig. 4. Estimated 857 GHz zodiacal emission templates, in MJy/sr, based on the model of K98, in Galactic coordinates, for Survey 1 (*left*), Survey 2 (*center*), and Survey 2 minus Survey 1 (*right*). From top to bottom we show dust band 1, dust band 2, dust band 3, the circumsolar ring, the Earth-trailing feature, and finally the diffuse cloud. Note that the scales for the *right-hand column* are different from those of the *left-hand* and *centre columns*, and that the scale for the bottom row is different from that of the others.

relics of asteroid collisions or collapses (Dermott et al. 1984; Sykes & Greenberg 1986). Reach et al. (1997) study them in detail.

The K98 model contains three bands[3] called Bands 1, 2, and 3. They appear at ecliptic latitudes ±1.°4, ±10°, and ±15°. IRAS, having higher angular resolution than DIRBE, found many bands, called α, β, γ, E/F, G/H, J/K, and M/N (Sykes 1990), though some are more firmly detected than others.

The K98 Band 1 (=IRAS Band γ), was originally associated with the Eos family of asteroids (Dermott et al. 1984), although Grogan et al. (2001) called this into question and Nesvorný et al. (2003, hereafter N03) found better correspondence with the Veritas family of asteroids.

K98 note that their Band 2 is a blend of IRAS Bands α and β (Sykes 1990). Sykes & Greenberg (1986) tentatively associated the α band with the Themis family of asteroids. Nesvorný et al. (2008, hereafter N08) has narrowed this association to a cluster within this family associated with the Beagle asteroid. The β band was associated by Sykes & Greenberg (1986) with the Koronis family of asteroids, and N03 narrowed this to the Karin cluster within the Koronis family. Anticipating the discussion in Sect. 6.4, we note also that the β band appears brighter than the α band (Sykes 1988; Reach et al. 1997; Nesvorný et al. 2008).

K98 states that their Band 3, that furthest from the ecliptic plane, has been associated with both the Io and Maria families of asteroids (Sykes 1988; Reach et al. 1997), corresponding to IRAS Bands J/K and M/N. N03 have more recently noted, however, that 4652 Iannini and/or 845 Naema may be better asteroid associations for the J/K band-pair, and that 1521 Seinajoki may work better for the M/N pair. We summarize these associations in Table 1.

For each of the three dust bands in the COBE model, the density is given by

$$n_B(\boldsymbol{R}) = \frac{3N_0}{R} e^{-(\zeta/\delta_\zeta)^6} \left(1 + \frac{(\zeta/\delta_\zeta)^p}{\upsilon_B}\right)(1 - e^{-(R/\delta_R)^{20}}), \quad (5)$$

where B denotes the band, and we have used a simplified notation based on that of K98, where one can also find the numerical values for the parameters. Note that Eq. (5) matches the code used for the zodiacal model (which can be found on the LAMBDA website), but that there is a factor of $1/\upsilon_B$ difference between Eqs. (5) and (8) of K98 (note that υ_B is a shape parameter, not a frequency). Also, K98 assumed that the emissivities of the three sets of bands were all equal. We relax this assumption below and allow the emissivities of each of the sets of bands to be different. The bands are shown, assuming unit emissivity, as the first, second, and third rows in Fig. 4.

4.1.3. Circumsolar ring and Earth-trailing feature

IPD particles drifting towards the Sun in their orbits can become trapped in orbital resonances near the Earth's orbit, thus creating a ring of enhanced density in these regions (Dermott et al. 1984). The functional form for the density of this circumsolar ring is taken to be

$$n_B(\boldsymbol{R}) = n_{\rm SR} \cdot e^{-(R-R_{\rm SR})^2/\sigma^2_{\rm rSR} - |Z_R|/\sigma_{\rm zSR}}. \quad (6)$$

Similar to the treatment of the bands, K98 assumed that the emissivity of the circumsolar ring was the same as that of the Earth-trailing feature, below. We also relax this assumption, and allow them to be different. The shape of the expected signal from the circumsolar ring is shown in the fourth row of Fig. 4.

The density of the Earth-trailing feature is given by

$$n_B(\boldsymbol{R}) = n_{\rm TB} \cdot e^{-(R-R_{\rm TB})^2/\sigma^2_{\rm rTB} - |Z_R|/\sigma_{\rm zTB} - (\theta-\theta_{\rm TB})^2/\sigma^2_{\theta\rm TB}}. \quad (7)$$

We note that for both the circumsolar ring and the Earth-trailing feature, there is an error in the text of K98 – a factor of 2 in the denominator of the first and third terms in the exponential has been added in the text, compared to what is in the code. We follow the code. The expected signal from the Earth-trailing feature is shown in the fifth row of Fig. 4.

4.1.4. Integrated emission

The total zodiacal emission is calculated as

$$I_x(\nu) = \epsilon_x \int d\boldsymbol{R} \cdot n_x(\boldsymbol{R}) \cdot B(\nu, T(\boldsymbol{R})), \quad (8)$$

where x is the zodiacal component, ν is the frequency, $\boldsymbol{R}$ is a location in the solar system, and $B(\nu, T(\boldsymbol{R}))$ is the *Planck* function for the frequency and temperature at the specific location, given by T_0/R^δ, with T_0 and δ being parameters. ϵ is the emissivity for the given component, which we will be finding with our fit, and n_x is the density for the given component, described above. The integral is carried out along the line of sight, from the location of the satellite to 5.2 AU.

4.2. Galactic emission seen through sidelobes

For the *Planck* telescope, we estimate a contribution to the total solid angle from far sidelobes – defined as beam response more than 5° from the centre of each beam (Planck Collaboration IV 2014; Planck Collaboration VII 2014) – of a fraction of a percent. Figure 5 shows the main far sidelobe paths.

The secondary reflector (SR) spillover arises from radiation that reaches the focal plane without reflecting off the primary reflector. As such, a major component is radiation from the general direction of the telescope boresight, though well outside the main beam. The "baffle" contribution to the SR spillover results from radiation that reflects off the baffles to arrive at the focal plane. The primary reflector (PR) spillover arises from radiation that comes to the satellite from just above the primary mirror, reflects off the secondary mirror and arrives at the detectors.

At the highest *Planck* frequencies, the Galactic centre is bright enough to be seen through the far sidelobes, even if faintly. Since the orientations of these sidelobes change as the instrument scans, the survey differences done to detect the zodiacal emission are also sensitive tests of the far side lobes. Though the Galactic emission mechanism and amplitude is different, analogous effects are discussed for the LFI in Planck Collaboration IV (2014).

To this point, resource constraints have limited this study to a single far sidelobe calculation for all detectors. We use a GRASP[4] calculation of the far sidelobes for the 353-1 horn (see Fig. 9 of Planck Collaboration VII 2014). The calculation is based on the multi-reflector, geometrical theory of diffraction and used backward ray-tracing. We do not attempt to correct for differences in either frequency or location for other horns. While this is not optimal, and will be improved in later releases, the primary, large-scale features of the far sidelobes are defined by the telescope, rather than the horns or their placement, so first-order effects

[3] While three bands are described in the text of K98, there are actually four in the code. There is, however, no ambiguity, as the density of the fourth band is set to zero in the code at the LAMBDA site.

[4] http://www.ticra.com/products/software/grasp

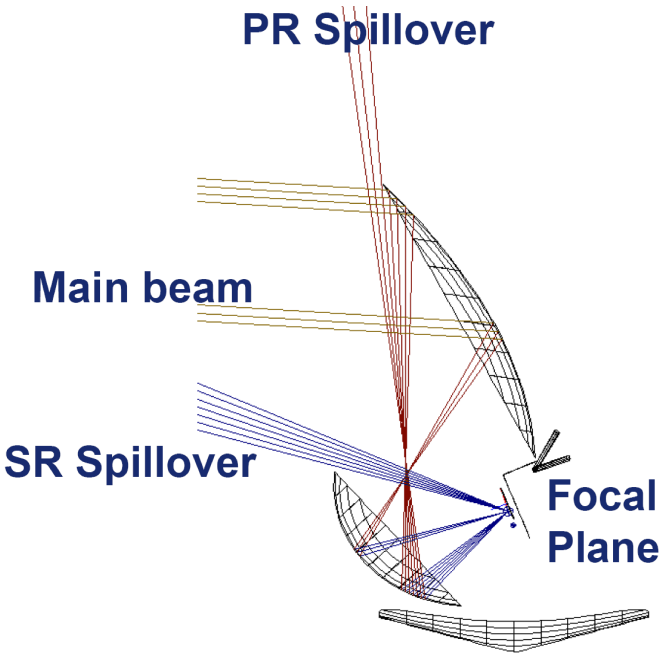

Fig. 5. Origin of far sidelobes. The "SR spillover" (for secondary reflector spillover; the lowest set of rays on the left of the figure) arrives at the focal plane from outside the secondary mirror, directly from the sky. The "PR spillover" (for primary reflector spillover), arrives at the focal plane from above the primary mirror and reflects off the secondary to arrive at the focal plane. The set of rays between these two contributions represents the main beam. The "baffle" contribution, light reaching the focal plane after reflecting from the inner sides of the baffles, is not shown here. It is often included as part of the SR Spillover. Adopted from Tauber et al. (2010).

should be captured. Some of the limitations imposed by this assumption are discussed in Sect. 6.1.

To make templates of what we might see from the Galactic centre through the far sidelobes, we use the *Planck* simulation software described in Reinecke et al. (2006), with the GRASP-calculated 353-1 far sidelobe pattern and the actual calibrated *Planck* frequency maps of the sky as inputs. The far sidelobe templates are made at the timeline level and run through the relevant parts of the pipeline software. In particular, the offset removal, or "destriping" must be done on the templates before fitting in order to obtain reasonable results. The templates made using these FSL calculations with a *Planck* 857 GHz sky as input are shown in the bottom three rows of Fig. 6.

One factor for which we do not account with these templates is the difference in spillover between the different frequencies (Lamarre et al. 2010; Tauber et al. 2010). Since we illuminate more of the telescope at lower frequencies than at higher frequencies, if our templates simply scale with the spillover, we would expect different fit values for our templates at different frequencies.

To illustrate the relative contributions of these various templates, Fig. 7 shows a series of maps. Maps in each row are similar to those in the previous row, except that one more template or group of templates has been added to form the new row. For all rows, the first column corresponds to data from Survey 1, the second column corresponds to Survey 2, and the third column is Survey 2 minus Survey 1. The first row shows the sum of all far sidelobes. The second row shows the result when we add Dust Band 1 to the far sidelobes – note that the scales change from the first to the second row. The third row shows the sum of the far sidelobes and Dust Bands 1 and 2. The fourth row shows the sum of the far sidelobes and all dust bands. The fifth row shows the fourth row plus the circumsolar ring and Earth-trailing feature. Finally, the bottom row shows the sum of the far sidelobes and all zodiacal templates (the scales have again changed). As this is simply illustrative, we have assumed unit emissivities for the zodiacal components, and multiplied the far sidelobe components by a factor of 15 (which we will see in Sect. 5 is representative of the most extreme case). With these caveats in mind, the survey difference of the sums of all the components, the lower right image, can be compared to the bottom image in Fig. 3. The zodiacal and far sidelobe structures can be seen in both figures. In addition to these, the largest differences are associated with the Galactic plane, where asymmetries in the main lobes plus beam orientation changes from one survey to the next will cause such signals.

5. Spectrum

We fit the data shown in the bottom panel of Fig. 3, as well as the analogous data at other frequencies and for the second year of observations, to a constant plus combinations of the templates shown in Figs. 4 and 6.

For each fit, we assume that the survey difference map at sky pixel p, called D_p, can be modelled as

$$D_p = \sum_t \left(\epsilon_{2,t} T_{2,t,p} - \epsilon_{1,t} T_{1,t,p}\right) + \text{constant}, \quad (9)$$

where $\epsilon_{[1|2],t}$ is the emissivity fit for template t during Survey 1 or 2 at the given frequency and $T_{[1|2],t,p}$ is the value of the tth template at pixel p for Survey 1 or 2, calculated as described in Sect. 4. For example, for our "basic" fit, we will have 19 templates – one each for the diffuse cloud, circumsolar ring, Earth-trailing feature, and each of the three dust bands, as well as one each for the Galactic far sidelobes. All of these are repeated twice, once for each survey in a yearly difference map. Finally we also fit to an overall constant, to which *Planck* is not sensitive. We then minimize

$$\chi^2 = \sum_p \left(\Delta_p - D_p\right)^2 . \quad (10)$$

Separating the templates into surveys has the disadvantage of increasing the number of parameters in our fits. While we do not expect either the emissivity of the zodiacal emission or the far sidelobe calculations to change from one survey to the next, we separate them in this way for two reasons. The first is simply as a basic reality check – if we see significant differences between fits to two different surveys, we should be sceptical. Beam asymmetries or transfer function effects, for example, might cause differences from survey to survey, as might imperfections in the model itself.

The second reason is to calculate uncertainties. As just noted, we are often as concerned by systemic effects as much as by "random" noise. By separating the data by survey, we may calculate uncertainties using the standard error of the successive measurements as a proxy for the uncertainties, rather than propagating white noise estimates. This should provide us with a more conservative estimate of our uncertainties, one that accounts for model deficiencies or low levels of systematics that change by survey (e.g., the aforementioned beam asymmetries and transfer functions).

The bulk of the zodiacal emission is, of course, in the ecliptic plane. *Planck*, on the other hand, has more statistical weight,

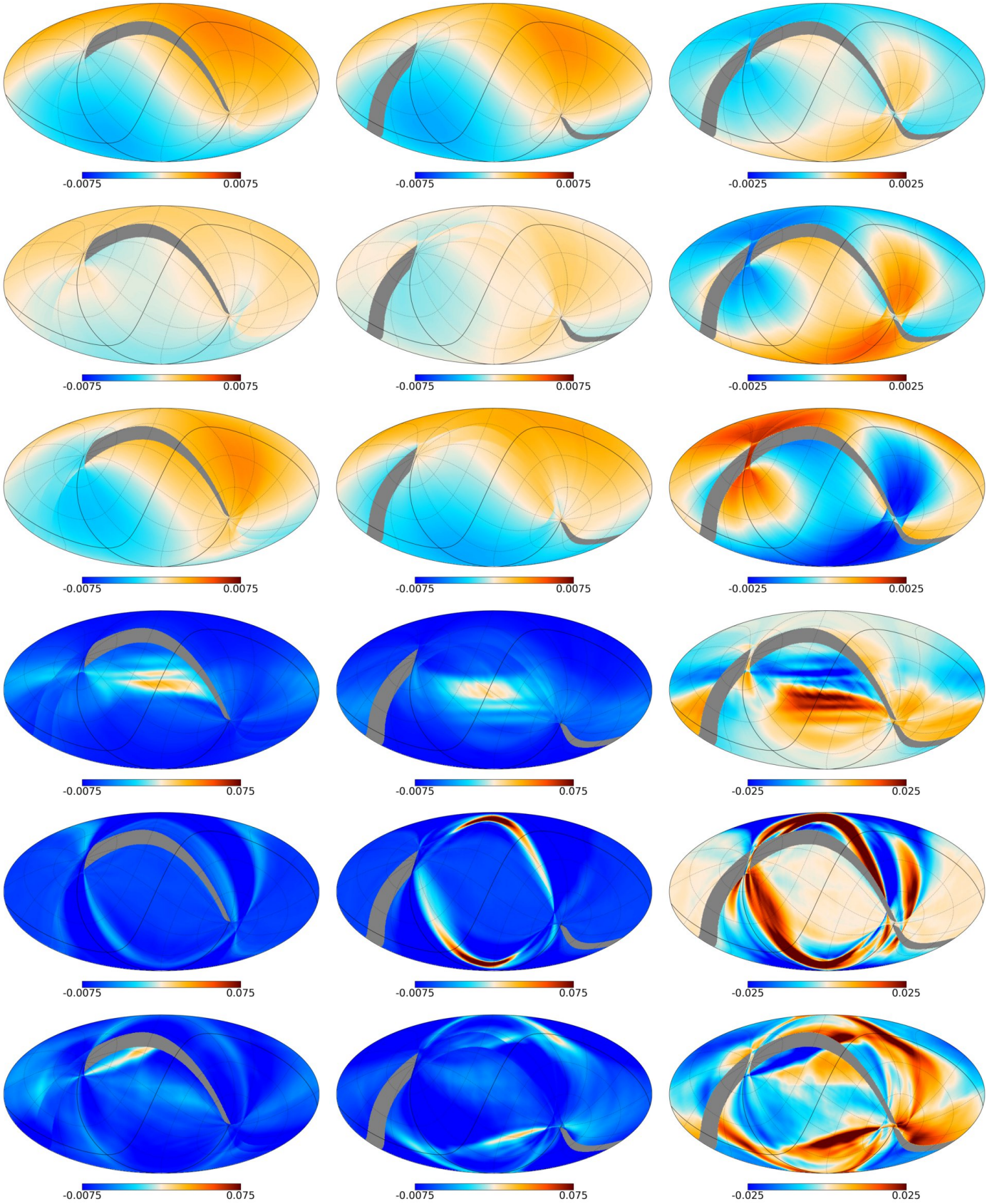

Fig. 6. Templates of the dipole and the Galaxy, in MJy/sr, seen through our far sidelobes for Surveys 1 (*left*) and 2 (*centre*), and for the difference in these two (*right*). *Row 1*: dipole seen through the direct SR contribution. *Row 2*: dipole seen through the PR contribution. *Row 3*: dipole seen through the baffle SR contribution. *Row 4*: galaxy seen through the direct SR contribution. *Row 5*: galaxy seen through the PR contribution. *Row 6*: galaxy seen through the baffle SR contribution. The simulations in *Rows 4–6* are made using 857 GHz data passed through the far sidelobe calculation described in Sect. 4.2. The scales are different for the top and bottom three rows, and for the first two and the last columns.

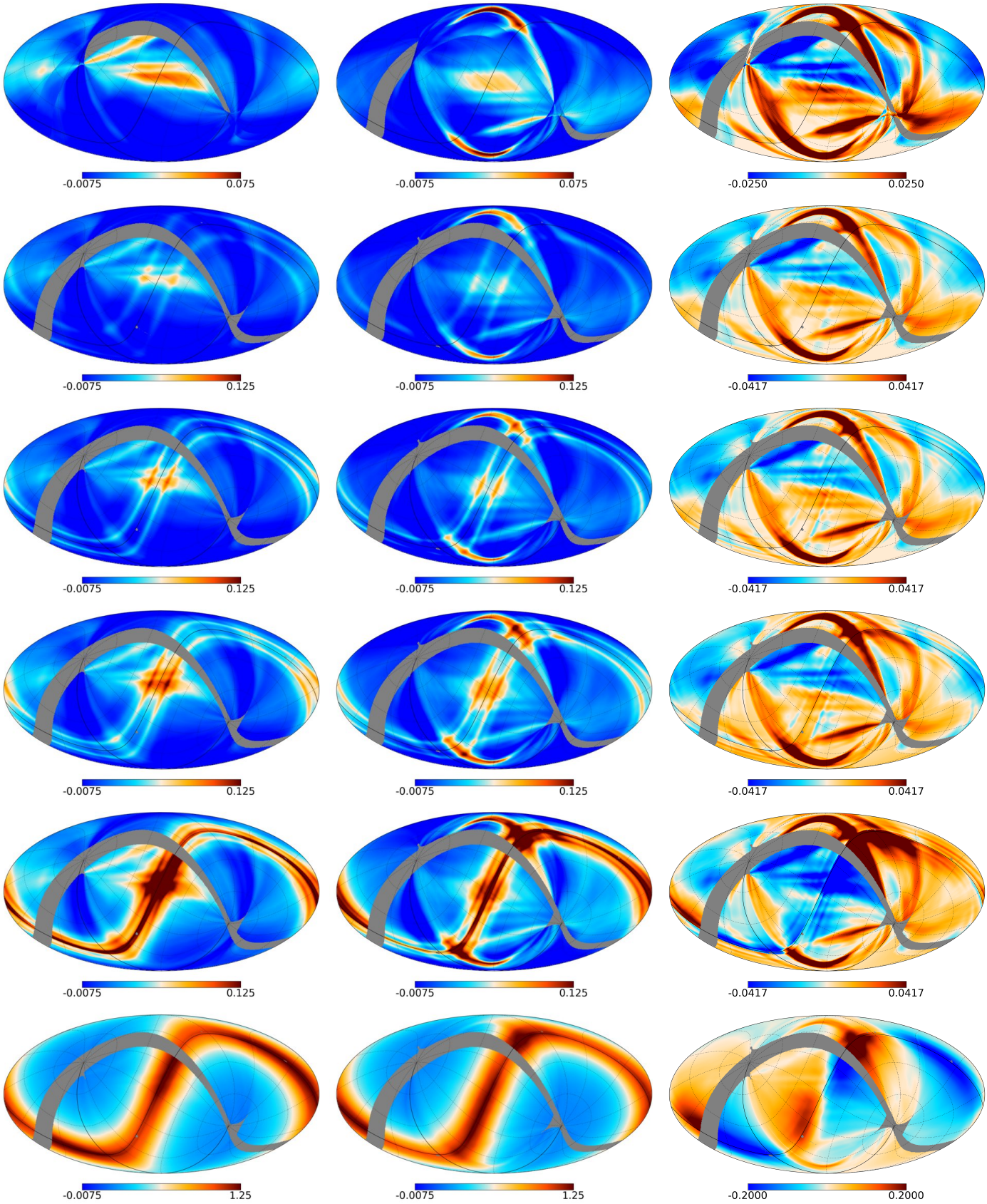

Fig. 7. Sequence of maps in MJy/sr, each building upon that above, designed to show the relative contributions of the various templates in Figs. 4 and 6. *Row 1*: The sum of the last three templates in Fig. 6. *Row 2*: Row 1 plus Dust Band 1. *Row 3*: Row 2 plus Dust Band 2. *Row 4*: Row 3 plus Dust Band 3. *Row 5*: Row 4 plus the circumsolar ring and Earth-trailing feature. *Row 6*: The far sidelobes and all zodiacal components. *Left*: Survey 1. *Centre*: Survey 2. *Right*: Survey 2 minus Survey 1. Note that the amplitudes used are only approximate, the figure being for illustrative purposes only. The scales change between the first and second rows, and between the fifth and sixth rows, as well as between the second and third column.

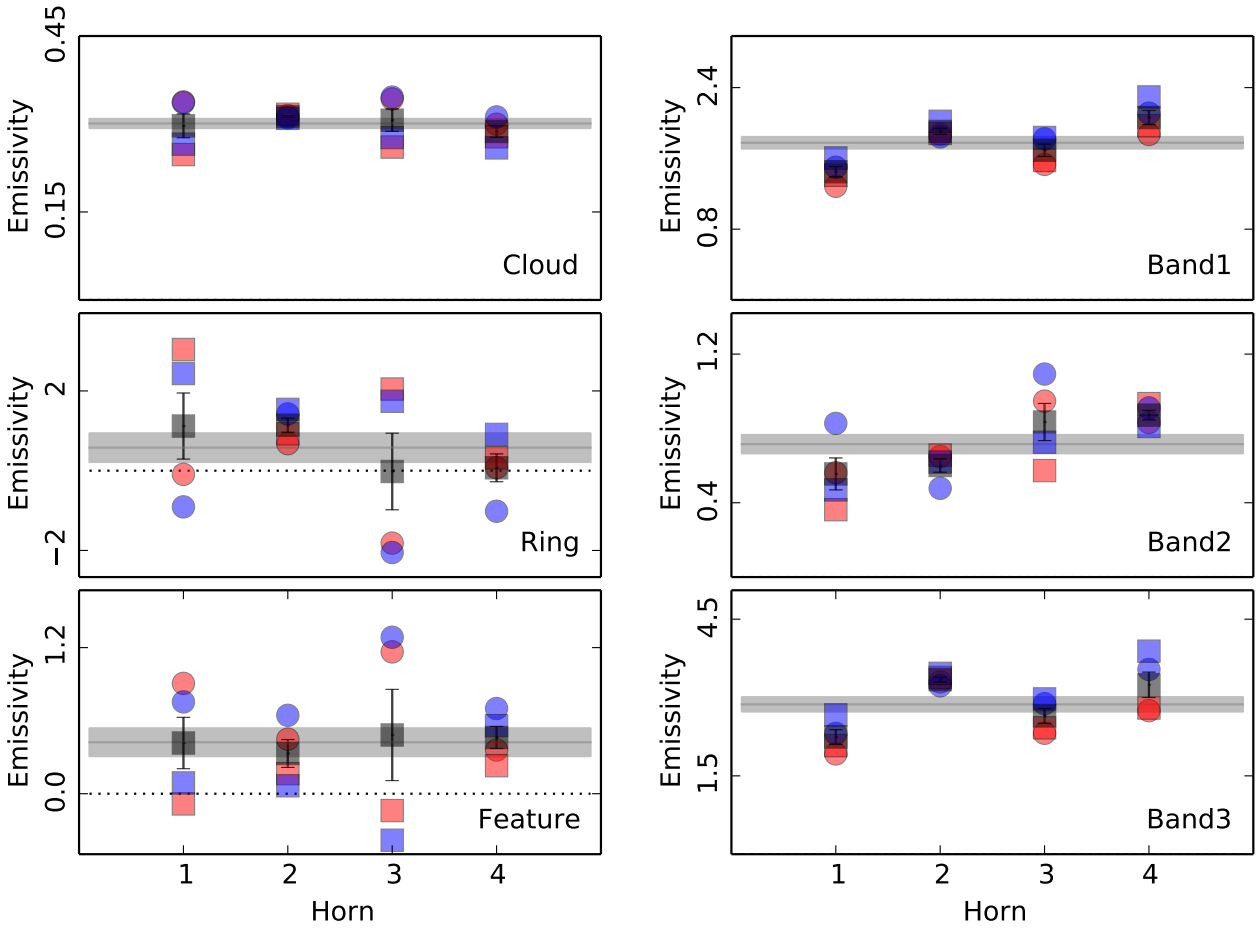

Fig. 8. Emissivities of components from fits at 857 GHz. Fits to the first year of *Planck* observations are in red, divided into Survey 1 (circles) and Survey 2 (squares). Fits to the second year are in blue, divided into Survey 3 (circles) and Survey 4 (squares). Absent time variability of the zodiacal emission, little difference would be expected between corresponding red and blue symbols. Agreement or disagreement between squares and circles gives some indication of systematic errors in the data and the correctness of the templates. The average of all measurements for each horn is shown as a black square, and the average and standard errors for the entire frequency, is given by the horizontal grey band. Dotted lines mark zero levels where appropriate. Similar plots for all HFI frequencies can be found in the *Planck* Explanatory Supplement (Planck Collaboration 2013).

pixel by pixel, at the ecliptic poles. We therefore use uniform weights over pixels, rather than statistical weights, since this would down-weight specifically the regions with our signal.

As mentioned above, we fit each of the survey difference maps to a cloud, circumsolar ring, Earth-trailing feature, three bands and three far sidelobe templates, plus a constant. The results for the four 857 GHz horns are shown in Fig. 8. Averaging over horns and surveys at all six HFI frequencies yields Fig. 9. Numerical values are given in Tables 2 and 3.

As discussed in the HFI processing paper (Planck Collaboration VI 2014) and in the *Planck* explanatory supplement (Planck Collaboration 2013), these fits are used to create the implied zodiacal and sidelobe emission in each HFI observation, which can then be removed from the data before the maps are recreated. Note that the fitted values are strictly used for the removal – even, for example, when they are negative. The Survey 2 minus Survey 1 difference maps for the 857-1 horn both with and without zodiacal and far sidelobe removal are shown in Figs. 10 and 11.

Inspection of the right-hand columns of Figs. 10 and 11 shows some artefacts of the aforementioned systematics, especially at submillimetre frequencies. In Table 4, we show the differences between emissivities measured from Surveys 2 and 4 and emissivities measured from Surveys 1 and 3, divided by the statistical uncertainty. To be more concrete, the first six entries in the 857 GHz (top) row compare the values of the circles with those of the squares in Fig. 8. Were there no systematic effects at all, we would expect these values to be of order 1. A larger number here is an indication there are either effects that need to be accounted for, or that the zodiacal or far sidelobe model may need improvement.

6. Discussion

Here we discuss the fit implications for both the HFI instrument and the zodiacal cloud.

6.1. Far sidelobes

In addition to fit values obtained for the Galaxy seen in each component of the far sidelobes, the columns labelled "Prediction" in Table 3 show the expected values of the spillover, normalized to that of the 353 GHz channel, from Tauber et al. (2010). These are the ratios of the expected spillover in each frequency, compared to that at 353 GHz, the frequency for which the sidelobe calculations were done. Since the fit values account for the changes in Galactic emission with frequency, if

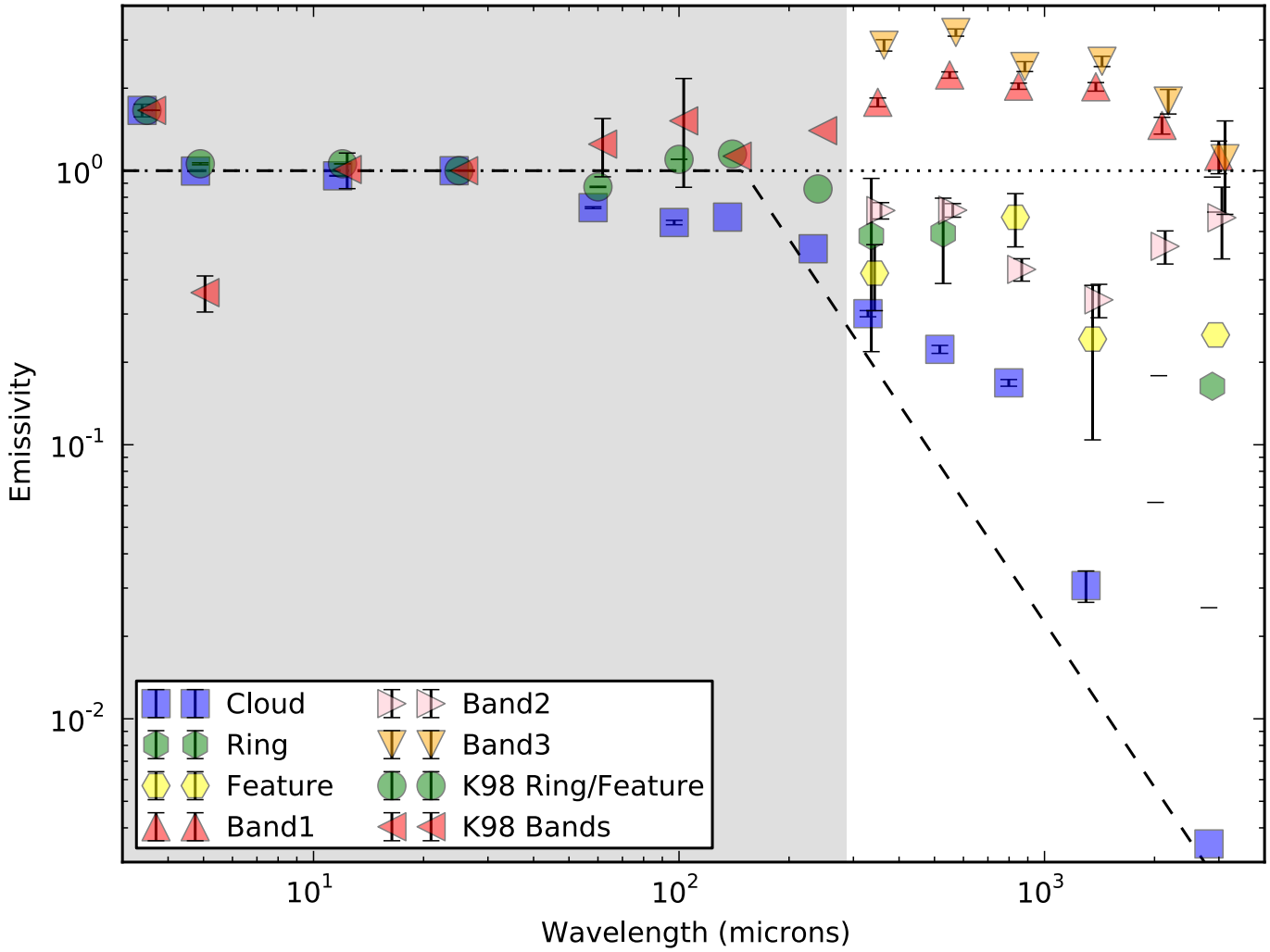

Fig. 9. Emissivities of components of the K98 zodiacal emission model obtained from *Planck*/HFI ($\lambda > 250\,\mu$m) and COBE/DIRBE ($\lambda \leq 250\,\mu$m, grey shading; K98). The diffuse cloud is shown as blue squares. For DIRBE, all dust bands (red, left-pointing triangles) were assumed have the same emissivity. For HFI, the bands (red, up-pointing triangles for Dust Band 1; pink, right-pointing triangles for Dust Band 2; and orange, down-pointing triangles for Dust Band 3) were allowed to have different emissivities. Similarly, K98 assumed that the circumsolar ring and Earth-trailing feature (green circles) had the same emissivities. For *Planck* the circumsolar ring (green hexagons) and Earth-trailing feature (yellow hexagons) were allowed to be different. *Planck* values were obtained by fitting an amplitude to each component, as well as the Galaxy seen through the sidelobes. All other parameters in the model were fixed at their K98 values. Each point is the average of the corresponding values obtained for all individual horns and surveys at the given frequency, over the first two years of HFI data (grey-shaded regions in each panel of Fig. 8. Error bars give the standard errors of these different measures. Numerical values are given in Table 2. Note that a few cloud, circumsolar ring, and Earth-trailing feature values are negative, and so do not appear in this log–log plot. In such cases, the upper limit will appear as a short horizontal line. The dotted line indicates an emissivity of unity at all wavelengths, and the dashed line indicates an emissivity that is unity at wavelengths below 150 μm and proportional to λ^{-2} at longer wavelengths.

our predictions and data were perfect, the fit values would match those of the predictions.

The FSL signature is clearly visible at 857 GHz in the bottom panel of Fig. 3, and quantified in Table 3. As the 857 and 545 GHz channels are multi-moded, the differences are not that surprising; unlike single-moded horns, multi-moded horns allow propagation of multiple, interacting electromagnetic modes. It is difficult to perform the calculations necessary for the prediction, since each mode must be accounted for, and each mode interacts with the others (Murphy et al. 2010). In addition, the specifications for the horn fabrication were quite demanding, and small variations could give large variations in the amount of spillover.

For the lower frequency, single-moded channels, however, the situation is different. There is no clear detection of PR spillover. While the significant negative values may indicate some low-level, large-scale systematic, there seems to be nothing with the distinctive signature of primary spillover at frequencies between 100 and 353 GHz.

For the direct contribution of the secondary SR spillover, the situation is similar at 353 GHz, but at 217 and 143 GHz we find a 3σ detection at about the level expected, while at 100 GHz the value is about 2.5 times higher than expected, though the signal-to-noise ratio of the detection is less than 2σ. The baffle contribution to the SR spillover seems to be in accord with expectations at 353 and 217 GHz, and higher than what is predicted at 100 GHz.

The values for the PR spillover, which is the most distinctive of the far sidelobe patterns and therefore presumably the easiest to disentangle from other effects, suggest that the PR spillover values in Table 2 of Tauber et al. (2010) may be slightly overestimated. The values for the direct contribution of the SR spillover roughly confirm the far sidelobe calculations.

Table 2. Emissivities of the zodiacal dust components from the fit result averages.

Frequency [GHz]	Emissivity					
	cloud	ring	feature	Band 1	Band 2	Band 3
857	0.301 ± 0.008	0.578 ± 0.359	0.423 ± 0.114	1.777 ± 0.066	0.716 ± 0.049	2.870 ± 0.137
545	0.223 ± 0.007	0.591 ± 0.203	−0.182 ± 0.061	2.235 ± 0.059	0.718 ± 0.041	3.193 ± 0.097
353	0.168 ± 0.005	−0.211 ± 0.085	0.676 ± 0.149	2.035 ± 0.053	0.436 ± 0.041	2.400 ± 0.100
217	0.031 ± 0.004	−0.185 ± 0.143	0.243 ± 0.139	2.024 ± 0.072	0.338 ± 0.047	2.507 ± 0.109
143	−0.014 ± 0.010	−0.252 ± 0.314	−0.002 ± 0.180	1.463 ± 0.103	0.530 ± 0.073	1.794 ± 0.184
100	0.003 ± 0.022	0.163 ± 0.784	0.252 ± 0.455	1.129 ± 0.154	0.674 ± 0.197	1.106 ± 0.413

Table 3. Fit coefficients for the Galaxy seen through the far sidelobes.

Frequency [GHz]	Primary spillover		Secondary spillover		
	fit	prediction[a]	direct	baffle	prediction[b]
100	−25.8 ± 5.7	7	26.3 ± 15.7	56.7 ± 5.7	10
143	−9.1 ± 4.1	6	13.0 ± 4.8	23.8 ± 5.4	10
217	0.6 ± 1.1	5	6.3 ± 2.1	6.5 ± 1.3	6
353	−1.2 ± 0.5	1	−4.3 ± 2.1	3.6 ± 0.7	1
545	7.7 ± 1.7	15	8.8 ± 3.1	7.9 ± 1.0	1
857	17.1 ± 3.4	1.5	23.9 ± 4.2	16.7 ± 3.1	0.005

Notes. [(a)] Unitless value we would expect for the fit to the primary spillover sidelobe contribution. It is the ratio of the primary spillover at the given frequency to the spillover at 353 GHz, as calculated in Table 2 of Tauber et al. (2010). If all our data and predictions were perfect, this value would match the corresponding value in the column labelled "Fit". [(b)] Unitless value we would expect for the fit to the secondary spillover sidelobe contribution. It is the ratio of the secondary spillover at the given frequency to the spillover at 353 GHz, as calculated in Table 2 of Tauber et al. (2010). If all our data and predictions were perfect, this value would match the corresponding fit values in the columns labelled "Direct" and "Baffle", which would also be equal to each other.

Table 4. Survey-to-survey consistency of the measurements.

Frequency [GHz]	$\sum_{d,y}\left(s_{d,2y}-s_{d,2y-1}\right)\left(e_{d,2y}^{-2}+e_{d,2y-1}^{-2}\right)^{-1/2}$								
	cloud	ring	feature	Band 1	Band 2	Band 3	PR	SR direct	SR baffle
857	−4.8	4.2	−5.1	0.7	−1.6	0.7	0.4	−0.3	−0.9
545	−3.1	2.7	1.1	1.2	−0.2	1.3	3.0	−1.0	−1.4
353	2.2	−0.5	−8.4	0.7	2.2	−0.1	−1.6	3.2	2.0
217	−1.4	5.4	−10.4	0.4	−0.2	0.4	−3.1	1.4	−0.5
143	−4.3	5.8	−1.1	0.4	−1.7	0.5	−2.1	1.1	0.2
100	−1.2	2.7	−3.2	0.2	−0.9	0.2	−2.2	2.4	0.4

Notes. For each component and frequency, the quantity $\sum_{d,y}\left(s_{d,2y}-s_{d,2y-1}\right)\left(e_{d,2y}^{-2}+e_{d,2y-1}^{-2}\right)^{-1/2}$ is given, where the sum is over years $y = 1, 2$ and all detectors d in a given frequency, and where $s_{d,2y}$ and $e_{d,2y}$ are the values and errors for emissivity measurements from even surveys. Quantities involving $2y - 1$ are the corresponding values for odd surveys. Thus, the entries in the tables are essentially the differences in fitted emissivities between even and odd surveys divided by the expected dispersion.

The baffle contribution to the SR spillover seems a bit high. We take the ensemble of these numbers as rough confirmation that our beam calculations are not drastically incorrect, but do not use the specific numbers in either Planck Collaboration VII (2014) or Planck Collaboration VIII (2014). Similar conclusions are drawn for the LFI in Planck Collaboration IV (2014).

The pre-launch optical system measurement campaign reinforces this conclusion. It found no significant SR baffle spillover excesses, or anything indicating a problem with the primary spillover calculations that might lead to significant, negative spillover values (Tauber et al. 2010). We attribute these numbers to systematics, perhaps linked with long time constants (Planck Collaboration VII 2014), which might move these large-scale features on the sky, or to the fact our sidelobe model has not accounted for the offset in the focal plane between the horn used to make the model and the 100 GHz horns.

We have also included a template of the dipole as seen through the far sidelobes in some fits to check if they are detected. As expected, they are not. The results quoted above are from fits that do not include these dipole templates.

6.2. Diffuse cloud

Figure 9 shows the emissivity of the diffuse cloud falling off with increasing wavelength, as would be expected for particles with characteristic sizes of order 30 μm. The dashed line shows a flat emissivity to 150 μm, with values proportional to the frequency squared at longer wavelengths. This is to aid comparison with

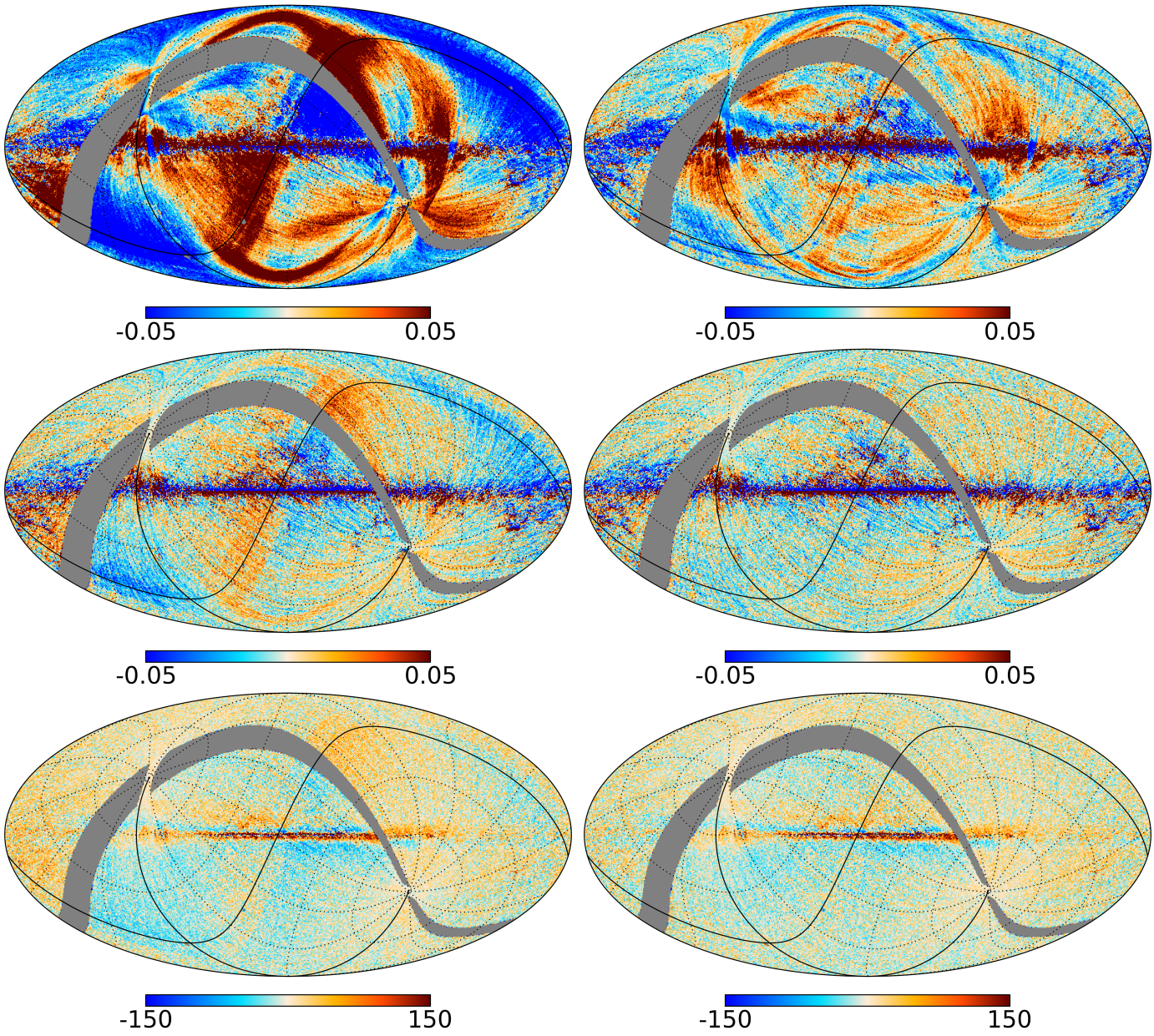

Fig. 10. Survey 2 minus Survey 1 difference maps, before (*left*) and after (*right*) zodiacal emission removal. *The top two rows*, for 857 and 545 GHz, are in units MJy sr^{-1}, while the *bottom row*, for 353 GHz, is in units of μK_{CMB}.

Fig. 2 of Fixsen & Dwek (2002), who used FIRAS data to investigate the far-infrared/submillimetre behaviour of the zodiacal cloud. Our results are consistent with their conclusions[5].

As the diffuse cloud is so much brighter in the mid-infrared than in the submillimetre, its relatively low level at *Planck* wavelengths has been exploited in Planck Collaboration IX (2014) to set in-flight limits on any possible out-of-band leaks in the instrument's spectral transmission.

6.3. Circumsolar ring and Earth-trailing feature

We draw no conclusions about the circumsolar ring or the Earth-trailing feature. The fit values obtained for their emissivities are inconsistent from frequency to frequency, and often negative. This remains true for *Planck* data even when the two components are required to have the same emissivities in the fit, as was done in K98.

This is not necessarily surprising, as the angle between the satellite spin axis and the direction of observation is less than 90°. This, in turn, means that in addition to observing deep in the Rayleigh-Jeans region of the dust spectrum, *Planck* rarely observes the centre of the circumsolar ring or Earth-trailing feature, which are nominally ≈90° from the Sun-Earth line, in contrast to IRAS and DIRBE, both of which often scanned through the regions of maximum density enhancement of the Ring and Feature.

Inspection of the middle- and lower-left panels of Fig. 8 shows systematic differences between results from even- and odd-numbered surveys (that is, the circles and squares seem to be systematically different, regardless of whether they are

[5] Care must be taken with direct comparisons between the emissivities quoted in Fixsen & Dwek (2002), who quote emissivities relative to a 245 K cloud, and those in this work, which follow K98 and assume a cloud of temperature 286 K at 1 AU from the Sun.

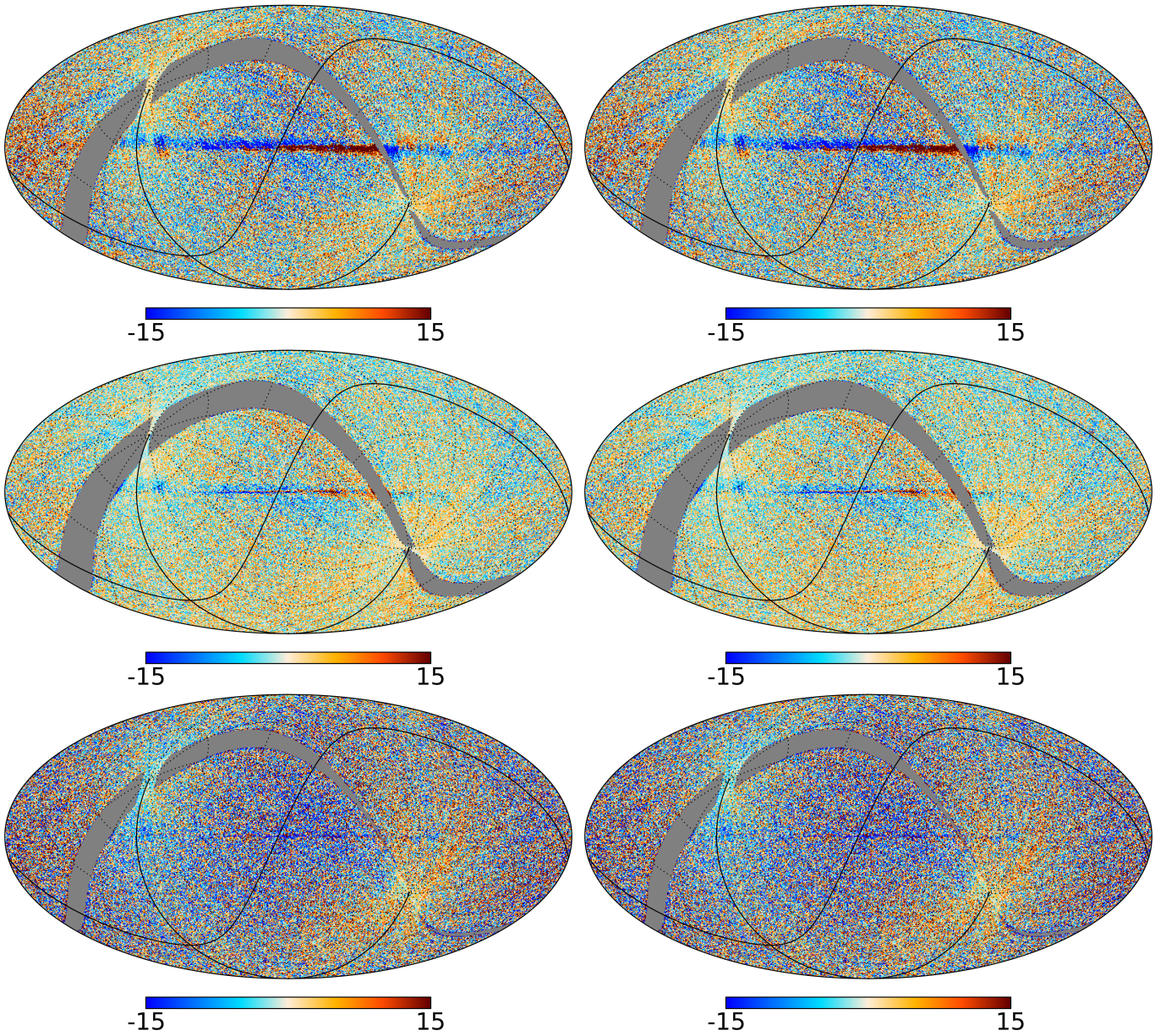

Fig. 11. Survey 2 minus Survey 1 difference maps before (*left*) and after (*right*) zodiacal emission removal. The rows, *from top to bottom*, are for 217, 143, and 100 GHz. All maps are in units of μK_{CMB}.

blue or red). *Planck*'s observing pattern was different for odd- and even-numbered surveys, but similar for even-numbered or odd-numbered surveys alone. Random noise is not important here, since the measurements with similar observations are repeatable, so this indicates either that the circumsolar ring and Earth-trailing model templates themselves need improvement at *Planck* wavelengths, particularly in the outer regions of the features sampled by *Planck*, or that systematic errors are affecting these specific components.

As the results for these components in particular are difficult to interpret, we have checked that the conclusions presented elsewhere in this work remain essentially the same whether or not we include the circumsolar ring and Earth-trailing feature.

6.4. Bands

An interesting feature of Fig. 9, and the primary result of this work, is the difference between the emissivities of the bands and that of the diffuse cloud. This indicates that the particles in the bands are larger than those in the diffuse cloud. While there may be hints of this in the longest wavelength DIRBE data, the effect becomes clear at *Planck* wavelengths. For Bands 1 and 3, the emissivity seems to cut off near $\lambda_{cutoff} \simeq 1$ mm. Since the cutoff is related to the characteristic particle size, a, as $\lambda_{cutoff} \simeq 2\pi a$, this would indicate a particle size of order 150 μm or greater. This can be compared to an implied characteristic size of around 30 μm for the particles in the diffuse cloud.

This is not unexpected. The composition of the diffuse cloud is disputed, but is often claimed to be both asteroidal and cometary (see, for example, Kortenkamp & Dermott 1998; Nesvorný et al. 2010; Tsumura et al. 2010). Since the bands, on the other hand, are understood to be asteroidal debris only (Sykes & Greenberg 1986), the difference may simply be a reflection of these different origins.

The fact that the fitted emissivities of Bands 1 and 3 rise above unity is perplexing. At first glance, one might imagine

some new, cold component in the cloud causing an enhancement that might be interpreted as an excess in emissivity in some other component. However, to peak around 545 GHz, this component would have to have a temperature of the order of 10 K, and therefore be much more distant than most of the dust usually associated with the zodiacal cloud. It is difficult to understand how such a component could survive the differencing process used in this analysis, which reduces signals from distant sources more than those nearby, or how such a component could mimic an excess in two dust bands above the ecliptic plane, but not do the same in the other zodiacal cloud components.

One might worry that covariance between between the various components might be causing problems in the fitting procedure. To check this, we have repeated the fit including and omitting various combinations of the the circumsolar ring and Earth-trailing feature, or both, and assuming their emissivities were independent or equal. In no case did the difference between the diffuse cloud and the dust bands disappear.

The excess may ultimately be explained by degeneracies in the model for the density of the bands. As presented in Sect. 4.1.2, the normalization of the density of particles is completely degenerate with the emissivity for each band. In addition, the emission is also roughly proportional to the temperature normalization, because we are observing in the Rayleigh-Jeans tail of the zodiacal emission. While any overall change in the temperature of the IPD particles would scale all components of the zodiacal emission, because temperature is nearly inversely proportional to the square-root of the distance from the Sun, the location of the bands is important. While the excess over unity is too large to be explained by errors in distance and thus temperatures alone, one might appeal to a change in a combination of distance, particle density normalization, and emissivity of these bands to arrive at mutually consistent results for both *Planck* and DIRBE. As this will involve a simultaneous study of both *Planck* and DIRBE data, it is beyond the scope of this paper.

Bands 1 and 3 also seem to show different behaviour than Band 2. Since Bands 1 and 3 are both at high ecliptic latitude, while Band 2 is not, one might again worry that one of the other templates to which we are fitting might have significant overlap with a subset of the bands, which in turn could cause an apparent difference in emissivities. To check this, we have repeated the fits with and without various combinations of the cloud, circumsolar ring, and Earth-trailing feature, as well as the far sidelobes. In all cases, Bands 1 and 3 are always significantly different than Dust Band 2. When the diffuse cloud itself is omitted from the fit, the emissivity of Dust Band 2 goes up, but is still distinctively different from that of Dust Bands 1 and 3.

As Dust Band 2 is a combination of the IRAS α and β bands, one may also worry that one of these two is more important for the shorter IRAS and COBE wavelengths, but that the other might be more important for the longer *Planck* wavelengths. We note that the Band 2 emission is dominated by contributions from the Karin/Koronis family (see Nesvorný et al. 2008, Fig. 1), but have therefore confirmed specifically that varying the δ_ζ parameter of the second band between values appropriate for either α or β does not remove this difference (see Table 1).

If the age of Band 2 was significantly different from those of Bands 1 and 3, we might argue that Poynting-Robertson drag had depleted some of the bands of more small particles than the others (Wyatt et al. 2011). N03 and N08, however, have estimated the ages of most of the asteroid families that might be associated with the bands (reproduced in Table 1), and the age of any of the associations with Band 2 is between those of any of the possible associations with Bands 1 or 3. These same figures tend to rule out modifications of the material properties due to photo-processing or solar wind exposure for differing periods. Band 2 also seems to be roughly the same distance from the Sun as the other two bands, so it is difficult to appeal to differences in environment as the cause.

We speculate on the following to explain any differences: Veritas, the asteroid family proposed to be associated with Dust Band 1, is classified as carbonaceous (Bus & Binzel 2002). As noted above, the IRAS β band, associated with the Karin family of asteroids, seems to dominate the emission from Dust Band 2. Karin and its larger sibling, Koronis, are classified as siliceous, or stony, objects (Bus & Binzel 2002; Carvano et al. 2010). While Dust Band 3 has a number of asteroid families that may be contributing to it (see Table 1), we propose that the emission is dominated by carbonaceous-based asteroid families (three quarters of the asteroids in the solar system are carbonaceous), and that the difference in emissivity between Dust Band 2 and Dust Bands 1 and 3 arises from this difference in composition. The differing emissivities may be either due to this intrinsic composition difference, or the size-frequency distribution of particles that results from different kinds of asteroids colliding (Grogan et al. 2001, for example). This explanation would not be valid, however, if it were to turn out that Dust Band 3 was dominated by dust associated with the Iannini asteroid, for example, since it is siliceous.

6.5. Implications for the CMB

Figure 12 shows the zodiacal emission implied by the fits, created by subtracting the maps made after applying the zodiacal emission correction from those that were made without the correction. One can see here the difference in the relative amplitudes of the bands versus the diffuse cloud, the bands being relatively more important at low than at high frequencies.

Figure 13 shows the power spectra of the zodiacal correction maps, all in units of $(\mu K_{CMB})^2$. Here, the cloud is seen at multipoles of less than about 10, while the bands and other structures are seen in higher multipoles.

At 143 GHz, the signal reaches a few μK_{CMB} in the map, while the power spectrum has values of the order of one $(\mu K_{CMB})^2$. The absence of power in the odd multipoles is a consequence of the north-south symmetry of the signal. While this pattern is reminiscent of the so-called "hemispheric anomaly" (Eriksen et al. 2004; Planck Collaboration XXIII 2014), we emphasize that the zodiacal emission is essentially symmetric about the ecliptic plane, while the anomalies exhibit anti-symmetries about the plane. Thus, standard zodiacal emission cannot be evoked to explain the anomalies. This is consistent with the conclusions of Dikarev et al. (2008).

The spectra in Fig. 13 can be compared with the CMB temperature anisotropy spectrum, which is shown as the black line about halfway between the top and bottom of the plot. The zodiacal emission correction spectra are orders of magnitude smaller than the CMB spectrum. The zodiacal emission therefore cannot compromise *Planck*'s cosmological results.

7. Conclusion

Zodiacal emission has long been an important foreground for searches for the extragalactic background at infrared wavelengths. With the ever-increasing sensitivity of CMB experiments, it will soon become important to account for at longer wavelengths as well.

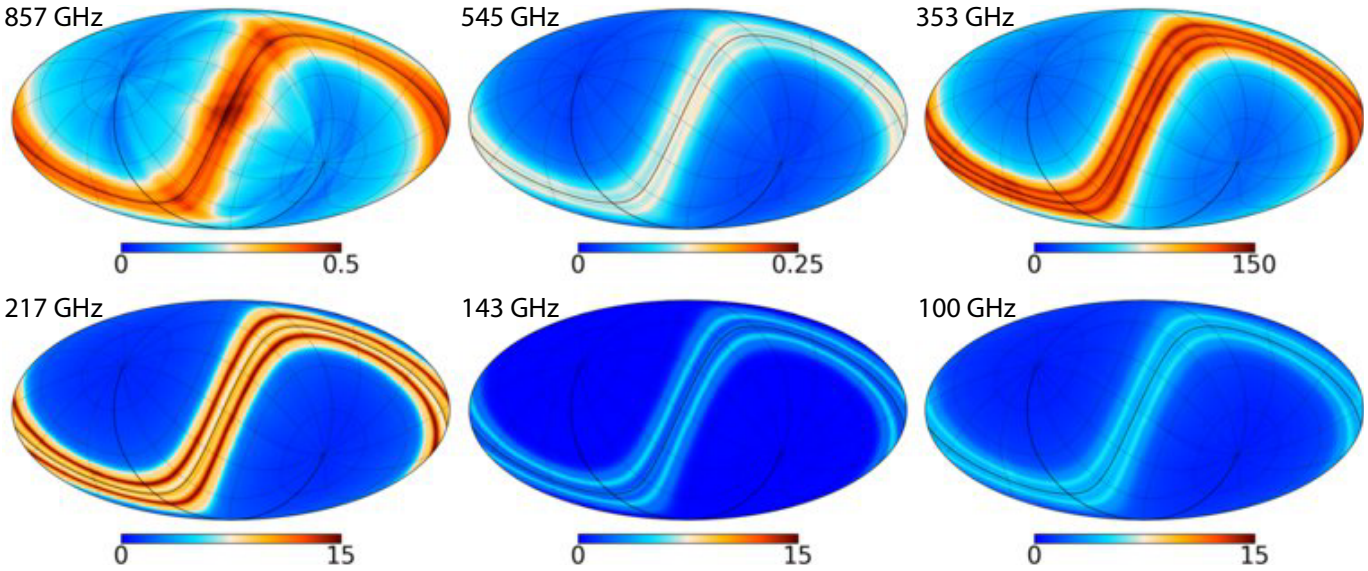

Fig. 12. Difference maps (uncorrected for zodiacal emission minus corrected) showing the zodiacal corrections calculated in this paper. Units are MJy/sr for 857 and 545 GHz, μK_{CMB} for the other frequencies.

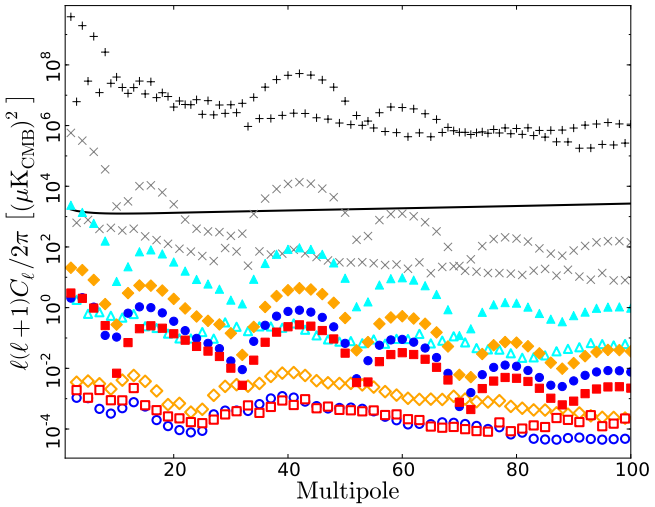

Fig. 13. Power spectra of the zodiacal correction maps shown in Fig. 12. Black plus signs = 857 GHz; grey crosses = 545 GHz; cyan triangles = 353 GHz; orange diamonds = 217 GHz; blue circles = 143 GHz; and red squares = 100 GHz. For the "CMB channels" 100–353 GHz, even multipoles are shown with filled symbols, odd multipoles with empty symbols. The "even-odd" pattern is a consequence of the symmetry around the ecliptic plane – odd multipoles are almost absent, as they would indicate structure in the maps that was anti-symmetric about the ecliptic plane. The best-fit ΛCDM CMB temperature anisotropy spectrum using the "Planck+WP+highL+BAO" data combination from Planck Collaboration XVI (2014), is shown as the solid line roughly half-way down the plot, orders of magnitude above the zodiacal spectrum in the *Planck* CMB channels.

The K98 model does fairly well in modelling the diffuse zodiacal cloud emission at *Planck* wavelengths, as long as appropriate emissivities are assumed. It does less well, however, in modelling the other features. Because they appear to be more emissive at these frequencies than the cloud, the bands contribute more to the zodiacal emission relative to the diffuse cloud at CMB frequencies (i.e., near 143 GHz = 2.1 mm). The 2013 *Planck* release includes both maps that have had zodiacal emission removed, and maps that have not had zodiacal emission removed.

We note that Planck Collaboration XI (2014) and Planck Collaboration Int. XVII (2014) found better results when using the *Planck* maps that had been cleaned of zodiacal emission, validating to some extent the zodiacal emission removal done here. Planck Collaboration XII (2014), on the other hand, used maps that had not had the zodiacal emission removed to make estimations of the CMB and other astrophysical components in the HFI maps. The component separation methods used there naturally correct for a large amount of zodiacal emission, as it is spectrally similar to Galactic dust emission in the *Planck* CMB channels. As might be expected, the differences between the dust maps obtained with the two different methods are explained by a consistent accounting of the zodiacal emission.

Improvements in modelling of the circumsolar ring, Earth-trailing feature, and the dust bands, as well as inclusion of fainter and partial bands (e.g., Espy et al. 2009) should be done to make truly "clean" CMB maps. As these bands are believed to be the products of asteroid collisions, further study of the bands at these wavelengths may also inform us about the nature of the intermediate-sized particles created during the destruction of the associated asteroids. We may hope to learn not only more about the size distribution, but also the differences between, for example, the results of collisions involving siliceous and carbonaceous asteroids.

Just as material from asteroid collisions contributes to zodiacal emission, material shed from comets must also contribute. As part of the HFI data reduction process, we mask out solar system objects that would cause "noise" in the final sky maps. We searched for comets as part of this process, but found only one (Christensen; see Appendix A). We have not yet detected extended tails of comets.

One of the primary goals of the next stage of analysis, once this "nearby" IPD has been completely removed, will be to search for or set limits on dust associated with the Kuiper belt. This will require total power maps rather than the differenced data used here, as the Kuiper belt is much farther away than the dust considered here and the amount of signal removed in the differencing process would be prohibitive. However, a beneficial

side effect of such analysis may be better limits on the IPD discussed here. Assuming that the noise after removing such effects is perfectly Gaussian and that Galactic contamination is mastered, *Planck* should be able to reduce the uncertainties in emissivities by a factor of roughly three for the diffuse cloud and Band 2, and by a factor of roughly eight for Bands 1 and 3. There would be only modest gains for the circumsolar ring, and the Earth-trailing feature would not be improved at all by moving to total power fits.

The full-mission *Planck* data release will include polarization information. While polarized zodiacal emission is not expected, limits will be put on possible contamination of the polarization of the CMB by such emission.

Work is now under way to address all these points for the next *Planck* data release. While the signal is quite small – at CMB wavelengths the signal we are discussing is orders of magnitude smaller than the primary CMB anisotropies – it is detectable and should be subtracted from the data. There will be improvements in dust modelling, improvements in satellite modelling, and additions to address polarization. The ultimate goal will be simultaneous analyses with IRAS, COBE, AKARI, and other data sets to understand the large-scale zodiacal emission from the near-infrared to the microwave.

Acknowledgements. This paper benefited from exchanges with Dale Fixsen, Tom Kelsall and Janet Weiland. We acknowledge the IN2P3 Computer Center (http://cc.in2p3.fr) for providing a significant amount of the computing resources and services needed for this work. We acknowledge the use of the Legacy Archive for Microwave Background Data Analysis (LAMBDA). Support for LAMBDA is provided by the NASA Office of Space Science. The development of *Planck* has been supported by: ESA; CNES and CNRS/INSU-IN2P3-INP (France); ASI, CNR, and INAF (Italy); NASA and DoE (USA); STFC and UKSA (UK); CSIC, MICINN, JA and RES (Spain); Tekes, AoF and CSC (Finland); DLR and MPG (Germany); CSA (Canada); DTU Space (Denmark); SER/SSO (Switzerland); RCN (Norway); SFI (Ireland); FCT/MCTES (Portugal); and PRACE (EU). A description of the *Planck* Collaboration and a list of its members, including the technical or scientific activities in which they have been involved, can be found at http://www.sciops.esa.int/index.php?project=planck&page=Planck_Collaboration

Appendix A: Solar system objects

Planck has detected many moving solar system objects, mostly asteroids, but also one comet. Most are masked at an early stage of the analysis so as not to affect the maps of the sky, thus they cannot be easily extracted from the delivered products. We therefore present them here.

Solar system objects are located using the JPL Horizons[6] (Giorgini et al. 1996) system programmed with the *Planck* orbit. Table A.1 shows the epochs of observation, and Tables A.2 and A.3 show the distance from the Sun and *Planck* at the time of observation, and the position on the sky.

During the standard HFI timeline processing, these objects are flagged and not included in the standard HFI maps (Planck Collaboration VI 2014), which makes these maps an excellent tool for removing the background of these moving objects.

5 Astraea, Christensen, and 128 Nemesis were not flagged in the maps, so their flux densities reported here have been adjusted for the fact that a fraction of their emission would have still been in the maps used to remove the background before estimating their fluxes.

We select time-ordered data within $0\overset{\circ}{.}5$ of the source and recalibrate into MJy sr^{-1} (using IRAS-conventions). We project the pointing of *Planck* into coordinates relative to the predicted position of the moving object. A synthetic background timeline is estimated by resampling the HEALPix-gridded (Górski et al. 2005) *Planck* maps using cubic spline interpolation.

We fit the main-beam template (Planck Collaboration VII 2014) for each bolometer to the time-ordered data. There are seven free parameters in the fit: x_0 and y_0, corresponding to the centroid of the object; a rotation angle ψ; an amplitude A; and three parameters describing a linear slope in x and y of any residual background. The amplitude times the solid angle of the beam model gives the flux density. Figure A.1 shows an example.

We find negligible difference between a fit assuming a Gaussian template for the beam instead of the PSF, as reported in Planck Collaboration VII (2014), so here we report the PSF-fit flux densities in Table A.4. We also tried aperture photometry, but the results were noisier and inconsistent from season-to-season, which might be expected, as the Ecliptic plane is somewhat under-sampled by *Planck*/HFI when using only a single season of data.

A.1. Notes

The residual map variance can change with different backgrounds. During its first observation period, for example, 1 Ceres was in a region of high foregrounds, and so was difficult to detect at 545 and 857 GHz, the bands most susceptible to foregrounds.

A.2. Basic behaviour

Figure A.2 demonstrates the basics of the asteroid flux density measurements: f is flux density, d is the distance between *Planck* and the object, and is the distance between the Sun and the object. Zero subscripts identifiy the first measurement for a given asteroid. The top panel shows asteroids detected in multiple surveys. Assuming the temperature of the object at any time goes as $s^{-1/2}$, we expect

$$f\, s^{1/2} \propto \frac{1}{d^2}, \tag{A.1}$$

which is roughly seen in the data.

In the bottom panel, we show the 545-to-857 GHz spectral indices, as well as the 545-to-353 GHz spectral indices for Ceres and Vesta.

[6] http://ssd.jpl.nasa.gov/?horizons

Table A.1. Dates of observation of solar system objects detected by *Planck*.

Object	Dates of observation				
	Season 1	Season 2	Season 3	Season 4	Season 5
1 Ceres	24/03/10–25/03/10	10/09/10–11/09/10	03/07/11–04/07/11	03/12/11–04/12/11	...
2 Pallas	23/02/10–25/02/10	30/07/10–31/07/10	02/05/11–03/05/11	13/10/11–15/10/11	...
3 Juno	10/12/09–12/12/09	30/12/10–01/01/11	27/05/11–28/05/11	...	...
4 Vesta	24/11/09–26/11/09	29/04/10–01/05/10	28/04/11–29/04/11	26/10/11–28/10/11	...
5 Astraea	05/10/09–06/10/09	30/07/10–31/07/10	02/01/11–03/01/11	27/12/11–28/12/11	...
6 Hebe	27/06/10–30/06/10	13/12/10–15/12/10	21/12/11–22/12/11	...	...
8 Flora	12/06/10–15/06/10	30/11/10–02/12/10	06/01/12–07/01/12	...	...
9 Metis	30/01/10–31/01/10	11/07/10–13/07/10	23/04/11–25/04/11	10/10/11–11/10/11	...
10 Hygiea	12/11/09–14/11/09	18/04/10–19/04/10	23/02/11–23/02/11	04/08/11–05/08/11	...
11 Parthenope	01/10/09–02/10/09	10/03/10–11/03/10	23/01/11–25/01/11	03/07/11–05/07/11	...
12 Victoria	20/02/10–21/02/10	15/08/10–16/08/10	09/09/11–11/09/11	21/09/11–21/09/11	...
13 Egeria	21/03/10–22/03/10	09/09/10–10/09/10	17/07/11–18/07/11	24/12/11–25/12/11	...
15 Eunomia	29/03/10–30/03/10	15/09/10–16/09/10	27/08/11–28/08/11	...	...
16 Psyche	18/10/09–19/10/09	16/09/10–17/09/10	01/03/11–01/03/11	23/12/11–24/12/11	...
17 Thetis	03/09/09–04/09/09	12/02/10–13/02/10	30/11/10–01/12/10	02/05/11–03/05/11	...
18 Melpomene	21/01/10–23/01/10	06/01/11–07/01/11	02/06/11–04/06/11	...	...
19 Fortuna	14/09/09–16/09/09	02/03/10–03/03/10	26/01/11–27/01/11	02/07/11–04/07/11	...
20 Massalia	13/12/09–15/12/09	28/12/10–30/12/10	03/06/11–05/06/11	...	...
29 Amphitrite	02/04/10–03/04/10	21/09/10–22/09/10	10/08/11–11/08/11	...	...
41 Daphne	27/11/09–28/11/09	28/08/10–28/08/10	03/02/11–04/02/11	05/11/11–07/11/11	...
45 Eugenia	19/04/10–20/04/10	06/10/10–07/10/10	06/08/11–07/08/11	11/01/12–12/01/12	...
52 Europa	23/09/09–24/09/09	05/03/10–06/03/10	14/01/11–15/01/11	21/06/11–23/06/11	...
88 Thisbe	08/11/09–09/11/09	25/09/10–26/09/10	03/03/11–03/03/11	06/12/11–06/12/11	16/12/11–16/12/11
128 Nemesis	24/09/09–25/09/09	05/03/10–06/03/10	05/01/11–07/01/11	06/06/11–08/06/11	...
324 Bamberga	03/10/09–04/10/09	12/03/10–14/03/10	02/01/11–04/01/11	25/05/11–26/05/11	...
511 Davida	19/02/10–20/02/10	31/07/10–01/08/10	01/04/11–02/04/11	07/09/11–08/09/11	...
704 Interamnia	18/02/10–19/02/10	03/08/10–04/08/10	16/04/11–17/04/11	01/10/11–02/10/11	...
Christensen	29/09/09–30/09/09	18/04/10–19/04/10	11/09/10–11/09/10	23/03/11–24/03/11	19/08/11–20/08/11

Table A.2. Location of solar system objects detected by *Planck*.

Object	Season	Solar range [AU]	*Planck* range [AU]	Ecliptic coordinates longitude [deg]	Ecliptic coordinates latitude [deg]
1 Ceres	1	2.774	2.536	271.1	2.17
1 Ceres	2	2.899	2.624	263.4	−4.66
1 Ceres	3	2.982	2.595	359.3	−11.99
1 Ceres	4	2.938	2.65	348.2	−11.24
2 Pallas	1	2.632	2.233	231.9	26.18
2 Pallas	2	2.994	2.807	218	35.55
2 Pallas	3	3.377	3.244	313.5	32.56
2 Pallas	4	3.403	3.137	297.9	24.6
3 Juno	1	2.051	1.667	356.8	−9.55
3 Juno	2	2.588	2.21	178.5	−3.66
3 Juno	3	2.959	2.615	165.4	3.95
4 Vesta	1	2.472	2.236	151.6	3.15
4 Vesta	2	2.325	1.872	143.3	8.00
4 Vesta	3	2.174	1.952	310.1	0.22
4 Vesta	4	2.318	1.966	311.1	−6.73
5 Astraea	1	3.065	2.7	294.2	0.92
5 Astraea	2	2.877	2.461	24.4	−4.22
5 Astraea	3	2.601	2.376	13.7	−5.69
5 Astraea	4	2.085	1.634	173.1	0.40
6 Hebe	1	2.062	1.611	356.3	−2.80
6 Hebe	2	1.945	1.537	0.6	−18.1
6 Hebe	3	2.648	2.239	166.3	1.85
8 Flora	1	2.089	1.695	345.6	−3.20
8 Flora	2	1.865	1.416	349	−7.85
8 Flora	3	2.363	1.986	186.3	5.42
9 Metis	1	2.448	2.017	207.6	6.15
9 Metis	2	2.619	2.42	199.1	2.71
9 Metis	3	2.635	2.463	305.8	−3.37
9 Metis	4	2.468	2.067	298.4	−6.37
10 Hygiea	1	3.245	3.09	141.5	−1.42
10 Hygiea	2	3.07	2.675	132	−3.25
10 Hygiea	3	2.795	2.455	235.1	−4.04
10 Hygiea	4	2.783	2.455	229.5	−2.32
11 Parthenope	1	2.531	2.303	98.1	−3.94
11 Parthenope	2	2.658	2.316	89.0	−1.31
11 Parthenope	3	2.633	2.222	200.7	4.42
11 Parthenope	4	2.489	2.255	192.2	5.08
12 Victoria	1	2.299	1.906	232.1	−4.83
12 Victoria	2	1.895	1.585	233.6	5.21
12 Victoria	3	2.386	2.181	78.8	0.36
12 Victoria	4	2.412	2.066	80.9	−0.10
13 Egeria	1	2.686	2.452	269.3	−7.48
13 Egeria	2	2.781	2.525	260.9	−15.85
13 Egeria	3	2.725	2.3	10.81	−16.19
13 Egeria	4	2.598	2.419	1.3	−6.08
15 Eunomia	1	2.928	2.737	278.5	−7.26
15 Eunomia	2	2.625	2.3	269.6	−0.21
15 Eunomia	3	2.146	1.877	63.7	13.24
16 Psyche	1	2.616	2.197	309.1	−0.06
16 Psyche	2	2.59	2.309	79.7	−3.43
16 Psyche	3	2.785	2.534	74.1	−2.76
16 Psyche	4	3.167	2.794	168.9	0.02

Table A.3. Location of solar system objects detected by *Planck*.

Object	Season	Solar range [AU]	*Planck* range [AU]	Ecliptic coordinates longitude [deg]	Ecliptic coordinates latitude [deg]
17 Thetis	1	2.707	2.379	64.0	−6.28
17 Thetis	2	2.799	2.62	53.7	−4.61
17 Thetis	3	2.643	2.394	155.5	0.79
17 Thetis	4	2.433	1.987	145.6	4.74
18 Melpomene	1	1.894	1.632	31.2	−11.75
18 Melpomene	2	2.66	2.279	184.3	2.54
18 Melpomene	3	2.792	2.47	169.8	7.48
19 Fortuna	1	2.067	1.709	77.4	−0.50
19 Fortuna	2	2.263	1.938	77.8	−1.70
19 Fortuna	3	2.757	2.354	203.5	−0.86
19 Fortuna	4	2.828	2.612	192	0.04
20 Massalia	1	2.301	1.983	357.8	−0.01
20 Massalia	2	2.154	1.743	177.3	−0.77
20 Massalia	3	2.384	2.015	171.7	−0.19
29 Amphitrite	1	2.725	2.532	283.5	−6.53
29 Amphitrite	2	2.638	2.3	276.7	−5.86
29 Amphitrite	3	2.406	2.121	44.2	2.69
41 Daphne	1	3.226	2.903	345.7	−1.72
41 Daphne	2	3.516	3.223	56.7	−11.57
41 Daphne	3	3.461	3.335	43.1	−14.57
41 Daphne	4	2.986	2.639	122.8	−17.39
45 Eugenia	1	2.551	2.362	300.8	5.51
45 Eugenia	2	2.679	2.279	296.1	1.39
45 Eugenia	3	2.901	2.661	41.1	−5.7
45 Eugenia	4	2.945	2.607	30.9	−7.41
52 Europa	1	2.847	2.62	88.9	−7.08
52 Europa	2	2.771	2.462	82.8	−3.53
52 Europa	3	2.906	2.525	191.7	5.93
52 Europa	4	3.065	2.841	183.3	7.74
88 Thisbe	1	2.391	1.964	329.2	6.14
88 Thisbe	2	2.901	2.667	89.4	2.67
88 Thisbe	3	3.108	2.838	78.6	−0.01
88 Thisbe	4	3.216	2.981	159.3	−3.99
88 Thisbe	5	3.213	2.828	160.4	−4.32
128 Nemesis	1	2.493	2.23	89.5	−1.29
128 Nemesis	2	2.683	2.356	83.0	3.43
128 Nemesis	3	3.022	2.671	184.5	7.05
128 Nemesis	4	3.091	2.801	172.6	6.19
324 Bamberga	1	1.993	1.675	98.0	13.12
324 Bamberga	2	2.572	2.204	92.5	7.13
324 Bamberga	3	3.398	3.059	181	−3.52
324 Bamberga	4	3.566	3.227	165.4	−6.94
511 Davida	1	3.422	3.071	228.5	17.37
511 Davida	2	3.626	3.496	217.5	13.4
511 Davida	3	3.756	3.595	280.3	6.68
511 Davida	4	3.717	3.349	268	1.34
704 Interamnia	1	3.498	3.201	230.6	−17.46
704 Interamnia	2	3.381	3.248	219.7	−12.38
704 Interamnia	3	3.053	2.907	297.9	−0.61
704 Interamnia	4	2.806	2.43	289.8	10.38
Christensen	1	3.235	2.864	290.7	22.74
Christensen	2	4.137	4.038	300.2	−10.42
Christensen	3	5.066	4.911	261.8	−24.26
Christensen	4	6.385	6.318	273.7	−34.56
Christensen	5	7.408	7.222	245.3	−40.48

Table A.4. Flux density of solar system objects detected at $\geq 3\sigma$ significance, using PSF fitting.

Object	Frequency	Flux density [Jy; IRAS convention]			
		Season 1	Season 2	Season 3	Season 4
1 Ceres	857	...	17.1 ± 0.1	17.7 ± 0.1	16.1 ± 0.1
1 Ceres	545	...	6.72 ± 0.11	7.51 ± 0.08	6.68 ± 0.11
1 Ceres	353	2.6 ± 0.5	2.52 ± 0.15	2.99 ± 0.09	2.5 ± 0.1
2 Pallas	857	8.9 ± 0.1	5.08 ± 0.07	3.05 ± 0.09	4.2 ± 0.1
2 Pallas	545	4.31 ± 0.11	2.27 ± 0.15	...	...
2 Pallas	353	1.7 ± 0.2	...	...	...
3 Juno	857	2.96 ± 0.07	1.79 ± 0.23	0.99 ± 0.13	...
3 Juno	545	1.13 ± 0.36	...	...	...
4 Vesta	857	7.39 ± 0.07	9.32 ± 0.07	10.1 ± 0.1	8.29 ± 0.06
4 Vesta	545	2.9 ± 0.1	3.55 ± 0.09	3.96 ± 0.09	3.18 ± 0.08
4 Vesta	353	1.3 ± 0.2	1.58 ± 0.32	1.8 ± 0.2	1.2 ± 0.2
6 Hebe	857	1.9 ± 0.1	1.52 ± 0.09	...	...
8 Flora	857	1.19 ± 0.11	1.78 ± 0.09	...	...
9 Metis	857	1.19 ± 0.19	...	...	1.06 ± 0.24
10 Hygiea	857	2.5 ± 0.1	4.03 ± 0.11	4.5 ± 0.1	4.56 ± 0.09
10 Hygiea	545	1.18 ± 0.17	1.61 ± 0.24	1.81 ± 0.25	2.11 ± 0.15
12 Victoria	857	...	1.11 ± 0.23	...	...
13 Egeria	857	...	...	...	1.17 ± 0.16
15 Eunomia	545	...	...	1.7 ± 0.3	...
16 Psyche	857	1.18 ± 0.38	...	...	...
18 Melpomene	857	1.05 ± 0.27	...	...	...
19 Fortuna	857	2.63 ± 0.11	1.47 ± 0.21	1.1 ± 0.2	...
20 Massalia	857	...	0.93 ± 0.22	...	...
29 Amphitrite	857	...	...	0.91 ± 0.17	...
45 Eugenia	857	1.54 ± 0.28	1.21 ± 0.19	...	...
52 Europa	857	2.81 ± 0.12	3.38 ± 0.26	2.05 ± 0.12	1.57 ± 0.11
52 Europa	545	1.08 ± 0.26	...	...	...
88 Thisbe	857	1.59 ± 0.33	...	...	...
128 Nemesis	857	1.4 ± 0.3	...	...	...
324 Bamberga	857	2.8 ± 0.1	1.79 ± 0.13	...	...
511 Davida	857	...	...	1.07 ± 0.32	...
704 Interamnia	857	1.61 ± 0.29	1.42 ± 0.17	2.19 ± 0.16	1.88 ± 0.15
Christensen	857	2.6 ± 0.2	...	...	...

Notes. Uncertainties include statistical errors of the PSF fit only, and should be added in quadrature to a calibration error of 1%, 5%, and 5% at 353, 545, and 857 GHz, respectively.

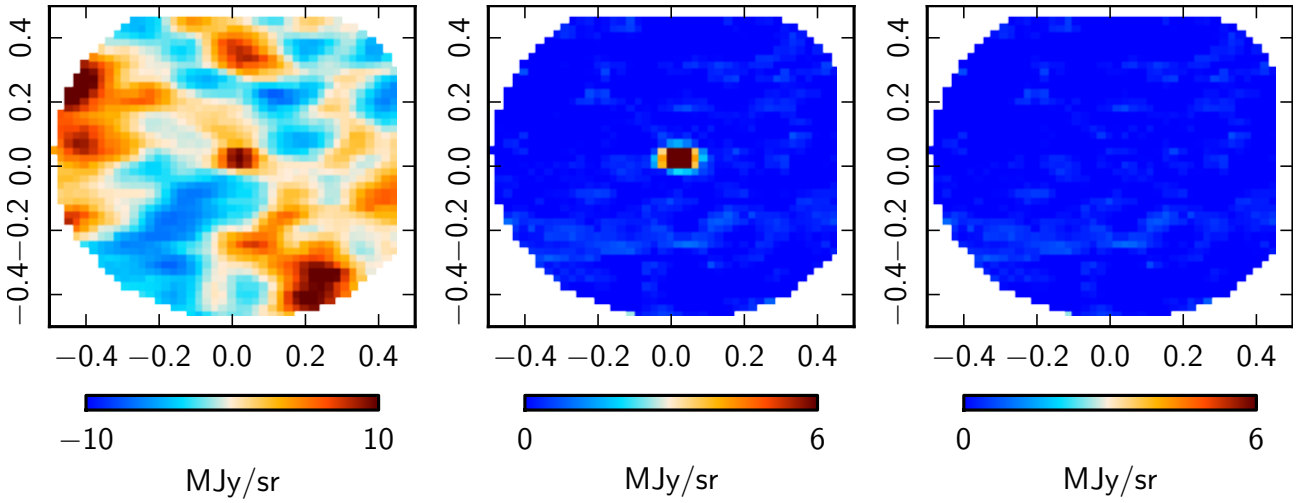

Fig. A.1. Example PSF fitting. Background removal and fitting are done in the time domain, bolometer by bolometer. These stacked maps were created only for visualization. *Left*: stacked data for the second observation season of 1 Ceres at 857 GHz, before background removal. *Center*: stacked data after background removal. *Right*: stacked data after background and source removal.

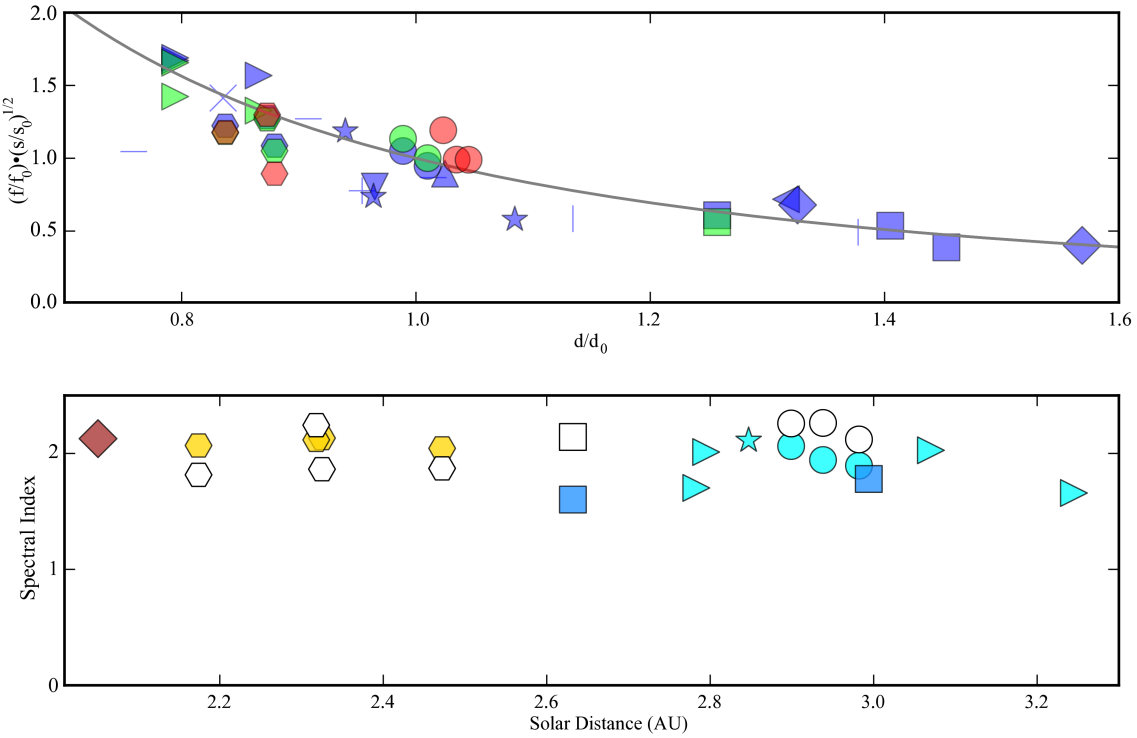

Fig. A.2. *Top*: ratio of $f\,s^{1/2}$ of the first and subsequent measurements for those solar system objects that were detected in more than one survey. Measurements at 857 GHz are shown in blue, measurements at 545 GHz are shown in green, and measurements at 353 GHz are shown in red. The grey line shows $(d/d_0)^{-2}$, which one would expect for Rayleigh-Jeans objects. *Bottom*: spectral index for those asteroids detected in multiple frequency bands for a given survey, defined as $\log(I_{545}/I_{857})/\log(545/857)$. Juno and Vesta are shown in brown and yellow, to indicate that they have different spectral classifications than Ceres, Pallas, Hygiea and Europa, shown in shades of blue. The white symbols show the corresponding values for 353–545 GHz, where they exist. For both panels, the symbols used for each object are: 1 Ceres – circles; 2 Pallas – squares; 3 Juno – diamonds; 4 Vesta – hexagons; 6 Hebe – +; 8 Flora – ×; 9 Metis – upward-pointing triangle; 10 Hygiea – right-pointing triangles; 19 Fortuna – vertical lines; 45 Eugenia – downward-pointing triangles; 52 Europa – stars; 324 Bamberga – left-pointing triangle; and 704 Interamnia – horizontal lines.

References

Bus, S. J., & Binzel, R. P. 2002, Icarus, 158, 146
Carvano, J. M., Hasselmann, P. H., Lazzaro, D., & Mothé-Diniz, T. 2010, A&A, 510, A43
Dermott, S. F., Nicholson, P. D., Burns, J. A., & Houck, J. R. 1984, Nature, 312, 505
Diego, J. M., Cruz, M., González-Nuevo, J., et al. 2010, MNRAS, 402, 1213
Dikarev, V., Preuß, O., Solanki, S., Krüger, H., & Krivov, A. 2008, Earth Moon Planets, 102, 555
Eriksen, H. K., Hansen, F. K., Banday, A. J., Górski, K. M., & Lilje, P. B. 2004, ApJ, 605, 14
Espy, A. J., Dermott, S. F., Kehoe, T. J. J., & Jayaraman, S. 2009, Planet. Space Sci., 57, 235
Fixsen, D. J., & Dwek, E. 2002, ApJ, 578, 1009
Giorgini, J. D., Yeomans, D. K., Chamberlin, A. B., et al. 1996, in BAAS, 28, 1158
Good, J. C., Gautier, T. N., & Hauser, M. G. 1986, Adv. Space Res., 6, 83
Górski, K. M., Hivon, E., Banday, A. J., et al. 2005, ApJ, 622, 759
Grogan, K., Dermott, S. F., & Durda, D. D. 2001, Icarus, 152, 251
Hansen, M., Kim, J., Frejsel, A. M., et al. 2012, J. Cosmol. Astropart. Phys., 10, 59
Hauser, M. G., Gillett, F. C., Low, F. J., et al. 1984, ApJ, 278, L15
Jones, M. H., & Rowan-Robinson, M. 1993, MNRAS, 264, 237
Jones, W. C., Bhatia, R., Bock, J. J., & Lange, A. E. 2003, in SPIE Conf. Ser. 4855, eds. T. G. Phillips, & J. Zmuidzinas, 227
Kelsall, T., Weiland, J. L., Franz, B. A., et al. 1998, ApJ, 508, 44
Kortenkamp, S. J., & Dermott, S. F. 1998, Icarus, 135, 469
Lamarre, J., Puget, J., Ade, P. A. R., et al. 2010, A&A, 520, A9
Leinert, C., Bowyer, S., Haikala, L. K., et al. 1997, VizieR Online Data Catalog, J/A+AS/127/1
Low, F. J., Young, E., Beintema, D. A., et al. 1984, ApJ, 278, L19
Maris, M., Burigana, C., & Fogliani, S. 2006, A&A, 452, 685
Maris, M., Burigana, C., Gruppuso, A., Finelli, F., & Diego, J. M. 2011, MNRAS, 415, 2546
Murphy, J., Peacocke, T., Maffei, B., et al. 2010, Multi-mode horn design and beam characteristics for the Planck satellite, Tech. Rep. JINST 5 T04001, IOP Publishing for SISSA
Nesvorný, D., Bottke, W. F., Levison, H. F., & Dones, L. 2003, ApJ, 591, 486
Nesvorný, D., Bottke, W. F., Vokrouhlický, D., et al. 2008, ApJ, 679, L143
Nesvorný, D., Jenniskens, P., Levison, H. F., et al. 2010, ApJ, 713, 816
Planck Collaboration I. 2011, A&A, 536, A1
Planck Collaboration 2013, The Explanatory Supplement to the Planck 2013 results, http://www.sciops.esa.int/wikiSI/planckpla/index.php?title=Main_Page (ESA)
Planck Collaboration I. 2014, A&A, 571, A1
Planck Collaboration II. 2014, A&A, 571, A2
Planck Collaboration III. 2014, A&A, 571, A3
Planck Collaboration IV. 2014, A&A, 571, A4
Planck Collaboration V. 2014, A&A, 571, A5
Planck Collaboration VI. 2014, A&A, 571, A6
Planck Collaboration VII. 2014, A&A, 571, A7
Planck Collaboration VIII. 2014, A&A, 571, A8
Planck Collaboration IX. 2014, A&A, 571, A9
Planck Collaboration X. 2014, A&A, 571, A10
Planck Collaboration XI. 2014, A&A, 571, A11
Planck Collaboration XII. 2014, A&A, 571, A12
Planck Collaboration XIII. 2014, A&A, 571, A13
Planck Collaboration XIV. 2014, A&A, 571, A14
Planck Collaboration XV. 2014, A&A, 571, A15
Planck Collaboration XVI. 2014, A&A, 571, A16
Planck Collaboration XVII. 2014, A&A, 571, A17
Planck Collaboration XVIII. 2014, A&A, 571, A18
Planck Collaboration XIX. 2014, A&A, 571, A19
Planck Collaboration XX. 2014, A&A, 571, A20
Planck Collaboration XXI. 2014, A&A, 571, A21
Planck Collaboration XXII. 2014, A&A, 571, A22
Planck Collaboration XXIII. 2014, A&A, 571, A23
Planck Collaboration XXIV. 2014, A&A, 571, A24
Planck Collaboration XXV. 2014, A&A, 571, A25
Planck Collaboration XXVI. 2014, A&A, 571, A26
Planck Collaboration XXVII. 2014, A&A, 571, A27
Planck Collaboration XXVIII. 2014, A&A, 571, A28
Planck Collaboration XXIX. 2014, A&A, 571, A29
Planck Collaboration XXX. 2014, A&A, 571, A30
Planck Collaboration XXXI. 2014, A&A, 571, A31
Planck Collaboration Int. XVII. 2014, A&A, 566, A55
Planck HFI Core Team 2011, A&A, 536, A6
Pyo, J., Ueno, M., Kwon, S. M., et al. 2010, A&A, 523, A53
Reach, W. T., Franz, B. A., Weiland, J. L., et al. 1995, Nature, 374, 521
Reach, W. T., Franz, B. A., & Weiland, J. L. 1997, Icarus, 127, 461
Reinecke, M., Dolag, K., Hell, R., Bartelmann, M., & Enßlin, T. A. 2006, A&A, 445, 373
Rowan-Robinson, M., & May, B. 2013, MNRAS, 429, 2894
Rowan-Robinson, M., Hughes, J., Vedi, K., & Walker, D. W. 1990, MNRAS, 246, 273
Rowan-Robinson, M., Jones, M., Leech, K., Vedi, K., & Hughes, J. 1991, MNRAS, 249, 729
Sykes, M. V. 1988, ApJ, 334, L55
Sykes, M. V. 1990, Icarus, 85, 267
Sykes, M. V., & Greenberg, R. 1986, Icarus, 65, 51
Tauber, J. A., Norgaard-Nielsen, H. U., Ade, P. A. R., et al. 2010, A&A, 520, A2
Tsumura, K., Battle, J., Bock, J., et al. 2010, ApJ, 719, 394
Vrtilek, J. M., & Hauser, M. G. 1995, ApJ, 455, 677
Wright, E. L. 1998, ApJ, 496, 1
Wyatt, M. C., Clarke, C. J., & Booth, M. 2011, Celest. Mech. Dyn. Astron., 111, 1

[1] APC, AstroParticule et Cosmologie, Université Paris Diderot, CNRS/IN2P3, CEA/lrfu, Observatoire de Paris, Sorbonne Paris Cité, 10 rue Alice Domon et Léonie Duquet, 75205 Paris Cedex 13, France
[2] Aalto University Metsähovi Radio Observatory, Metsähovintie 114, 02540 Kylmälä, Finland
[3] African Institute for Mathematical Sciences, 6-8 Melrose Road, 7945 Muizenberg, Cape Town, South Africa
[4] Agenzia Spaziale Italiana Science Data Center, via del Politecnico snc, 00133 Roma, Italy
[5] Agenzia Spaziale Italiana, Viale Liegi 26, 00198 Roma, Italy
[6] Astrophysics Group, Cavendish Laboratory, University of Cambridge, J J Thomson Avenue, Cambridge CB3 0HE, UK
[7] Astrophysics & Cosmology Research Unit, School of Mathematics, Statistics & Computer Science, University of KwaZulu-Natal, Westville Campus, Private Bag X54001, 4000 Durban, South Africa
[8] Atacama Large Millimeter/submillimeter Array, ALMA Santiago Central Offices, Alonso de Cordova 3107, Vitacura, Casilla 763 0355 Santiago, Chile
[9] CITA, University of Toronto, 60 St. George St., Toronto, ON M5S 3H8, Canada
[10] CNRS, IRAP, 9 Av. colonel Roche, BP 44346, 31028 Toulouse Cedex 4, France
[11] California Institute of Technology, Pasadena, California, USA
[12] Centre for Theoretical Cosmology, DAMTP, University of Cambridge, Wilberforce Road, Cambridge CB3 0WA, UK
[13] Centro de Estudios de Física del Cosmos de Aragón (CEFCA), Plaza San Juan, 1, planta 2, 44001 Teruel, Spain
[14] Computational Cosmology Center, Lawrence Berkeley National Laboratory, Berkeley, California, USA
[15] Consejo Superior de Investigaciones Científicas (CSIC), 28006 Madrid, Spain
[16] DSM/Irfu/SPP, CEA-Saclay, 91191 Gif-sur-Yvette Cedex, France
[17] DTU Space, National Space Institute, Technical University of Denmark, Elektrovej 327, 2800 Kgs. Lyngby, Denmark
[18] Département de Physique Théorique, Université de Genève, 24 quai E. Ansermet, 1211 Genève 4, Switzerland
[19] Departamento de Física Fundamental, Facultad de Ciencias, Universidad de Salamanca, 37008 Salamanca, Spain
[20] Departamento de Física, Universidad de Oviedo, Avda. Calvo Sotelo s/n, 33007 Oviedo, Spain
[21] Department of Astronomy and Astrophysics, University of Toronto, 50 Saint George Street, Toronto, Ontario, Canada
[22] Department of Astrophysics/IMAPP, Radboud University Nijmegen, PO Box 9010, 6500 GL Nijmegen, The Netherlands
[23] Department of Electrical Engineering and Computer Sciences, University of California, Berkeley, California, USA
[24] Department of Physics & Astronomy, University of British Columbia, 6224 Agricultural Road, Vancouver, British Columbia, Canada

[25] Department of Physics and Astronomy, Dana and David Dornsife College of Letter, Arts and Sciences, University of Southern California, Los Angeles, CA 90089, USA
[26] Department of Physics and Astronomy, University College London, London WC1E 6BT, UK
[27] Department of Physics, Florida State University, Keen Physics Building, 77 Chieftan Way, Tallahassee, Florida, USA
[28] Department of Physics, Gustaf Hällströmin katu 2a, University of Helsinki, 00014 Helsinki, Finland
[29] Department of Physics, Princeton University, Princeton, New Jersey, USA
[30] Department of Physics, University of California, Berkeley, California, USA
[31] Department of Physics, University of California, One Shields Avenue, Davis, California, USA
[32] Department of Physics, University of California, Santa Barbara, California, USA
[33] Department of Physics, University of Illinois at Urbana-Champaign, 1110 West Green Street, Urbana, Illinois, USA
[34] Dipartimento di Fisica e Astronomia G. Galilei, Università degli Studi di Padova, via Marzolo 8, 35131 Padova, Italy
[35] Dipartimento di Fisica e Scienze della Terra, Università di Ferrara, via Saragat 1, 44122 Ferrara, Italy
[36] Dipartimento di Fisica, Università La Sapienza, P.le A. Moro 2, 00185 Roma, Italy
[37] Dipartimento di Fisica, Università degli Studi di Milano, via Celoria, 16, 20133 Milano, Italy
[38] Dipartimento di Fisica, Università degli Studi di Trieste, via A. Valerio 2, Trieste, Italy
[39] Dipartimento di Fisica, Università di Roma Tor Vergata, via della Ricerca Scientifica 1, 00133 Roma, Italy
[40] Discovery Center, Niels Bohr Institute, Blegdamsvej 17, Copenhagen, Denmark
[41] Dpto. Astrofísica, Universidad de La Laguna (ULL), 38206 La Laguna, Tenerife, Spain
[42] European Southern Observatory, ESO Vitacura, Alonso de Cordova 3107, Vitacura, Casilla 19001 Santiago, Chile
[43] European Space Agency, ESAC, Planck Science Office, Camino bajo del Castillo, s/n, Urbanización Villafranca del Castillo, Villanueva de la Cañada, 28692 Madrid, Spain
[44] European Space Agency, ESTEC, Keplerlaan 1, 2201 AZ Noordwijk, The Netherlands
[45] Helsinki Institute of Physics, Gustaf Hällströmin katu 2, University of Helsinki, 00014 Helsinki, Finland
[46] INAF – Osservatorio Astrofisico di Catania, via S. Sofia 78, 95123 Catania, Italy
[47] INAF – Osservatorio Astronomico di Padova, Vicolo dell'Osservatorio 5, 35122 Padova, Italy
[48] INAF – Osservatorio Astronomico di Roma, via di Frascati 33, 00040 Monte Porzio Catone, Italy
[49] INAF – Osservatorio Astronomico di Trieste, via G.B. Tiepolo 11, 34131 Trieste, Italy
[50] INAF Istituto di Radioastronomia, via P. Gobetti 101, 40129 Bologna, Italy
[51] INAF/IASF Bologna, via Gobetti 101, 40129 Bologna, Italy
[52] INAF/IASF Milano, via E. Bassini 15, 20133 Milano, Italy
[53] INFN, Sezione di Bologna, via Irnerio 46, 40126 Bologna, Italy
[54] INFN, Sezione di Roma 1, Università di Roma Sapienza, Piazzale Aldo Moro 2, 00185 Roma, Italy
[55] IPAG: Institut de Planétologie et d'Astrophysique de Grenoble, Université Joseph Fourier, Grenoble 1/CNRS-INSU, UMR 5274, 38041 Grenoble, France
[56] IUCAA, Post Bag 4, Ganeshkhind, Pune University Campus, 411 007 Pune, India
[57] Imperial College London, Astrophysics group, Blackett Laboratory, Prince Consort Road, London, SW7 2AZ, UK
[58] Infrared Processing and Analysis Center, California Institute of Technology, Pasadena, CA 91125, USA
[59] Institut Néel, CNRS, Université Joseph Fourier Grenoble I, 25 rue des Martyrs, 38042 Grenoble, France
[60] Institut Universitaire de France, 103 bd Saint-Michel, 75005 Paris, France
[61] Institut d'Astrophysique Spatiale, CNRS (UMR 8617), Université Paris-Sud 11, Bât. 121, 91405 Orsay, France
[62] Institut d'Astrophysique de Paris, CNRS (UMR 7095), 98bis boulevard Arago, 75014 Paris, France
[63] Institute for Space Sciences, 77125 Bucharest-Magurale, Romania
[64] Institute of Astronomy and Astrophysics, Academia Sinica, Taipei, Taiwan
[65] Institute of Astronomy, University of Cambridge, Madingley Road, Cambridge CB3 0HA, UK
[66] Institute of Theoretical Astrophysics, University of Oslo, Blindern, 0315 Oslo, Norway
[67] Instituto de Astrofísica de Canarias, C/Vía Láctea s/n, 38200 La Laguna, Tenerife, Spain
[68] Instituto de Física de Cantabria (CSIC-Universidad de Cantabria), Avda. de los Castros s/n, 39005 Santander, Spain
[69] Jet Propulsion Laboratory, California Institute of Technology, 4800 Oak Grove Drive, Pasadena, California, USA
[70] Jodrell Bank Centre for Astrophysics, Alan Turing Building, School of Physics and Astronomy, The University of Manchester, Oxford Road, Manchester, M13 9PL, UK
[71] Kavli Institute for Cosmology Cambridge, Madingley Road, Cambridge, CB3 0HA, UK
[72] LAL, Université Paris-Sud, CNRS/IN2P3, Orsay, France
[73] LERMA, CNRS, Observatoire de Paris, 61 Av. de l'Observatoire, 75014 Paris, France
[74] Laboratoire AIM, IRFU/Service d'Astrophysique – CEA/DSM – CNRS – Université Paris Diderot, Bât. 709, CEA-Saclay, 91191 Gif-sur-Yvette Cedex, France
[75] Laboratoire Traitement et Communication de l'Information, CNRS (UMR 5141) and Télécom ParisTech, 46 rue Barrault, 75634 Paris Cedex 13, France
[76] Laboratoire de Physique Subatomique et de Cosmologie, Université Joseph Fourier Grenoble I, CNRS/IN2P3, Institut National Polytechnique de Grenoble, 53 rue des Martyrs, 38026 Grenoble Cedex, France
[77] Laboratoire de Physique Théorique, Université Paris-Sud 11 & CNRS, Bât. 210, 91405 Orsay, France
[78] Lawrence Berkeley National Laboratory, Berkeley, California, USA
[79] Max-Planck-Institut für Astrophysik, Karl-Schwarzschild-Str. 1, 85741 Garching, Germany
[80] McGill Physics, Ernest Rutherford Physics Building, McGill University, 3600 rue University, Montréal, QC, H3A 2T8, Canada
[81] MilliLab, VTT Technical Research Centre of Finland, Tietotie 3, 02044 Espoo, Finland
[82] National University of Ireland, Department of Experimental Physics, Maynooth, Co. Kildare, Ireland
[83] Niels Bohr Institute, Blegdamsvej 17, 2100 Copenhagen, Denmark
[84] Observational Cosmology, Mail Stop 367-17, California Institute of Technology, Pasadena CA 91125, USA
[85] Optical Science Laboratory, University College London, Gower Street, London, UK
[86] SB-ITP-LPPC, EPFL, 1015, Lausanne, Switzerland
[87] SISSA, Astrophysics Sector, via Bonomea 265, 34136 Trieste, Italy
[88] School of Physics and Astronomy, Cardiff University, Queens Buildings, The Parade, Cardiff, CF24 3AA, UK
[89] Space Sciences Laboratory, University of California, Berkeley, California, USA
[90] Special Astrophysical Observatory, Russian Academy of Sciences, Nizhnij Arkhyz, Zelenchukskiy region, 369167 Karachai-Cherkessian Republic, Russia
[91] Stanford University, Dept of Physics, Varian Physics Bldg, 382 via Pueblo Mall, Stanford, California, USA

[92] Sub-Department of Astrophysics, University of Oxford, Keble Road, Oxford OX1 3RH, UK
[93] Theory Division, PH-TH, CERN, 1211 Geneva 23, Switzerland
[94] UPMC Univ Paris 06, UMR 7095, 98 bis Boulevard Arago, 75014 Paris, France
[95] Université de Toulouse, UPS-OMP, IRAP, 31028 Toulouse Cedex 4, France
[96] Universities Space Research Association, Stratospheric Observatory for Infrared Astronomy, MS 232-11, Moffett Field CA 94035, USA
[97] University of Granada, Departamento de Física Teórica y del Cosmos, Facultad de Ciencias, 18071 Granada, Spain
[98] Warsaw University Observatory, Aleje Ujazdowskie 4, 00-478 Warszawa, Poland